

Chapter 2

The Imaging Atmospheric Cherenkov Technique and the IACTs MAGIC and CTA

In this chapter we will describe the concept behind the detection of gamma rays through the imaging atmospheric Cherenkov technique. We will also describe the IACT arrays on which this thesis focuses: the Major Atmospheric Gamma-ray Imaging Cherenkov (MAGIC) telescopes and the Cherenkov Telescope Array (CTA). The hardware and techniques used to analyze the data of MAGIC will be described in detail. We will give an overview of the CTA project, together with a brief description of the telescope types involved in the project.

2.1 The Imaging Atmospheric Cherenkov Technique

The EM spectrum spans more than 20 orders of magnitude in energy from radio to TeV gamma rays. The atmosphere is transparent to most of the radiation up to the UV, but higher energy photons do not penetrate into the atmosphere due to their interaction with the air molecules. A picture showing the bounds of the EM spectrum and the transparency of the atmosphere to all of them is shown in Fig. 2.1. To detect those photons, one has to use satellites where they have not been blocked yet. Unfortunately, due to the low fluxes, the collection area offered by satellites is not large enough at energies exceeding 100 GeV.

Due to the interaction with the atmospheric nuclei, VHE particles produce cascades, also known as EASs. As the relativistic charged particles produced in the cascade move faster than the speed of light in the atmosphere, they produce Cherenkov light at wavelengths ranging from IR to UV. In the following, we will give a more detailed description of the shower development in the atmosphere and the way we can detect the Cherenkov light using optical telescopes. For a more detailed review, see Engel et al. (2011).

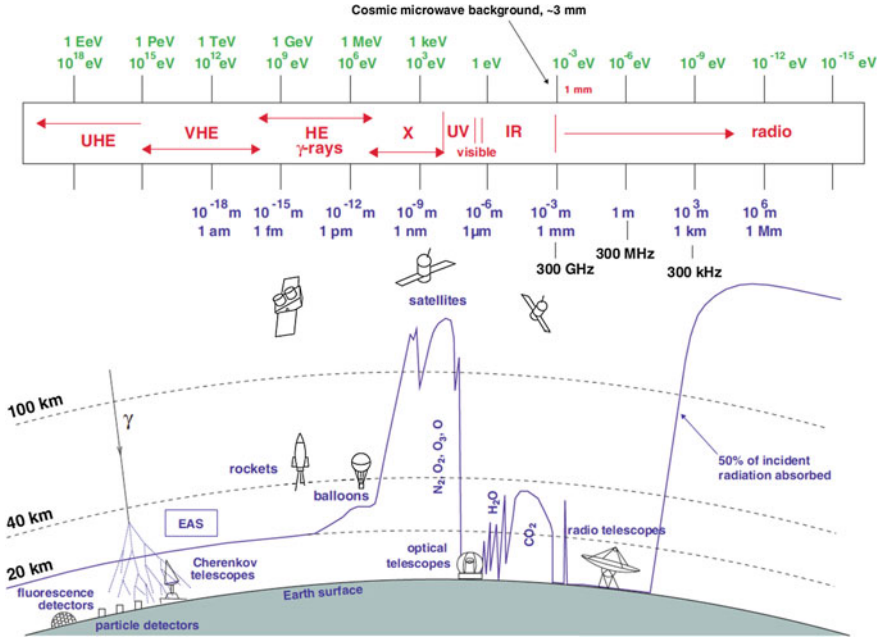


Fig. 2.1 The bounds of the EM spectrum (*above*) as seen from the altitude where photons are fully absorbed in the atmosphere (*below*). From Longair (1992), Moralejo (2000), Wagner (2006)

2.1.1 Types of Showers

To describe the particle interaction with the air nuclei it is better to describe the atmosphere in terms of the so-called *atmospheric depth* X , which is the product of particle density and distance or the amount of mass per unit of area that an incident particle encounters on its path. For vertical incidence, the atmospheric depth at sea level is $X_{\text{air}} \sim 1013 \text{ g cm}^{-2}$. We will describe the characteristics of the particle cascades produced depending on the primary particle initiating the shower.

2.1.1.1 EM Showers

When a gamma ray enters into the atmosphere, if its energy is $E \gtrsim 20 \text{ MeV}$, it undergoes e^{\pm} pair creation in the presence of an air nucleus. These e^{-} and e^{+} suffer bremsstrahlung if their energy exceeds the critical energy $E_C = 86 \text{ MeV}$, which is the energy for which energy losses by bremsstrahlung and ionization are equal. The bremsstrahlung process produces photons that are still very energetic, undergoing further pair production. Eventually, a so-called EM shower of e^{-} , e^{+} and gamma rays develops (see left panel of Fig. 2.2). The energy loss dE of an e^{-} with path dx due to bremsstrahlung can be written as:

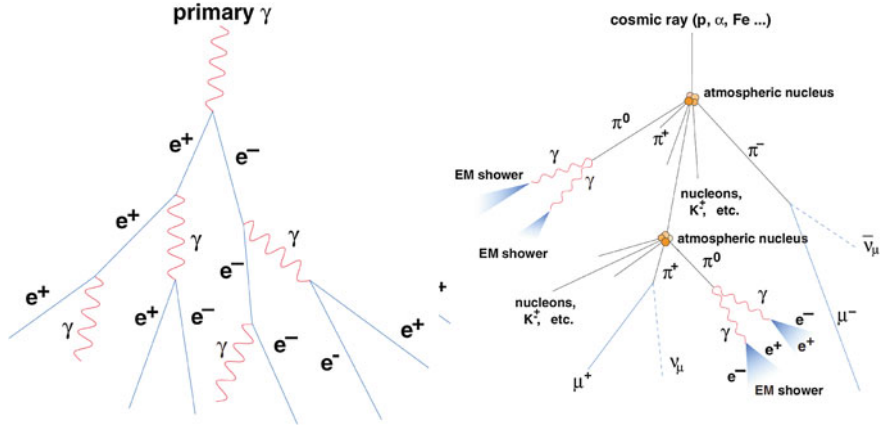


Fig. 2.2 Scheme of an EM (*left panel*) and hadronic (*right panel*) initiated showers. Taken from Wagner (2006)

$$\frac{dE}{dx} = -\frac{E}{X_0^e} \quad (2.1)$$

where $X_0^e = 37.2 \text{ g cm}^{-2}$ is the radiation length for an e^- (or e^+) in air. The radiation length of a γ -ray photon X_0^γ can be written as a function of that of the electron: $X_0^\gamma = 7/9 X_0^e$. An EM shower is roughly symmetric with respect to the shower axis. The first interaction point is not very dependent on the γ -ray energy and is situated at a height of about 20–30 km above sea level (a.s.l.) for a vertically incident particle. Roughly speaking, the number of particles is doubled each step of the cascade, and the energy of the particles halved. When the energy of e^\pm reaches E_C , the cascading stops and the number of particles is maximum. The height a.s.l. at which this condition is fulfilled is known as *height* of the shower maximum (H_{\max}). This height is inversely proportional to the logarithm of the energy $H_{\max} \propto 1/\ln(E)$ of the primary gamma ray.

2.1.1.2 Hadronic Showers

When the primary particle generating the EAS is a hadron, the first interaction with an atmospheric nucleus is governed by the strong force. In this process, mostly pions are created (90 %, in roughly equal proportions $\pi^0 : \pi^+ : \pi^- \rightarrow 1 : 1 : 1$) as well as kaons (10 %) and light baryons (p, \bar{p}, n, \bar{n}) in a much smaller proportion. Hadrons and pions undergo further collisions. The shower grows until the energy per nucleon reaches the minimum energy required for pion production decay ($\sim 1 \text{ GeV}$). In addition pions decay into photons, e^- , e^+ and muons, generating secondary EM and muon-initiated showers. The pionic and muonic decays involved in a hadronic shower are the following:

$$\begin{aligned}\pi^0 &\longrightarrow \gamma\gamma & \pi^+ &\longrightarrow \mu^+ \nu_\mu & \pi^- &\longrightarrow \mu^- \bar{\nu}_\mu \\ \mu^+ &\longrightarrow e^+ \nu_e \bar{\nu}_\mu & \mu^- &\longrightarrow e^- \bar{\nu}_e \nu_\mu\end{aligned}$$

As illustrated in the right panel of Fig. 2.2, several EM subcascades are generated. Apart from that, due to the strong interaction, the transverse momentum of secondary hadrons is larger than that of leptons in EM showers, therefore hadronic showers are wider.

The timing of the showers is also important to differentiate them. γ -ray initiated showers develop in less than 3 ns for impact parameters smaller than the hump (the region where the Cherenkov photon density is highest), while hadron-initiated ones take more than 10 ns to develop. Figure 2.3 shows MC simulations of two EASs produced by a gamma ray and a proton of the same energy. One can clearly see the γ -ray showers are more “beamed” than proton showers.

2.1.2 Cherenkov Light

The existence of Cherenkov light was first proposed by Pavel Cherenkov (1934). It is an effect produced by ultrarelativistic charged particles moving at a speed faster than the speed of light in the medium. A charged particle moving at a speed v in a medium with refraction index n , the medium polarizes along its track. If the speed of the particle is $v < c/n$, where c is the speed of light in vacuum, the polarization is symmetrical and no electric field is produced at long distances (see Fig. 2.4a). On the other hand, if the speed of the particle is $v > c/n$ it moves faster than the EM radiation that induces the polarization, which is not symmetric anymore as shown in Fig. 2.4b. To compensate the effect of a non-symmetric dipole medium, an EM shock wave called Cherenkov radiation is produced. This radiation is emitted in the form of a cone at an angle θ (see Fig. 2.4c) such as:

$$\cos \theta = \frac{c}{v n(\lambda)} \quad (2.2)$$

where $n(\lambda)$ is the spectral index of the medium, which depends on the wavelength of the Cherenkov light. The number of Cherenkov photons produced by an ultrarelativistic particle as a function of the length and wavelength is given by (Yao et al. 2006):

$$\frac{d^2 N}{dx d\lambda} = \frac{2\pi\alpha}{\lambda^2} \left(1 - \frac{c^2}{v^2 n^2(\lambda)} \right) \approx 370 \sin^2 \theta(\lambda) [\text{eV}^{-1} \text{cm}^{-1}] \quad (2.3)$$

where $\alpha \approx 1/137$ is the fine structure constant and λ the wavelength.

Cherenkov light produced in the atmosphere The cascades originated in the atmosphere contain several relativistic particles that travel faster than the speed of light in the atmosphere. The fact that showers should produce Cherenkov light was

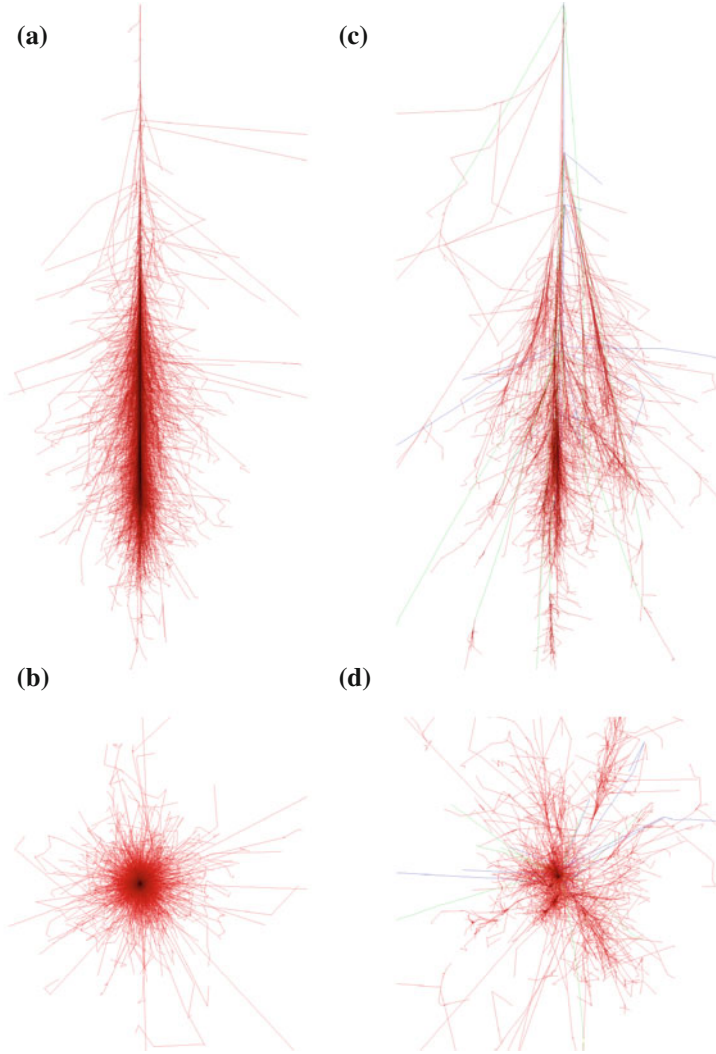


Fig. 2.3 *Upper left panel* 100 GeV γ -ray shower particle track. *Lower left panel* The same γ -ray shower seen on the transversal plane. *Upper right panel* 100 GeV proton shower particle track. *Lower right panel* The same proton shower seen on the transversal plane. Red lines correspond to e^- , e^+ and γ -ray tracks, green for muons and blue for hadrons. From Schmidt (2015)

pointed out by Blackett (1948) and later measured by Jelley and Porter (1963). According to the Cherenkov light propagation shown in Fig. 2.4c, a vertical incident ultrarelativistic particle illuminates a doughnut ring on the ground. The superposition of the rings generated by all the particles emitting Cherenkov light form a circle on the ground. Since $(n - 1) \sim \mathcal{O}(10^{-4})$ in the air, the maximum angle from Eq. 2.2 is $\theta \lesssim 1^\circ$.

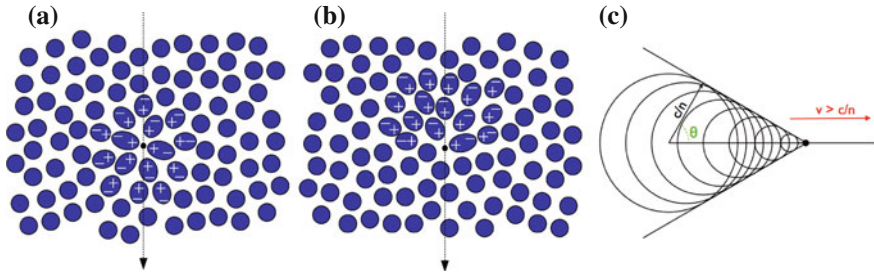


Fig. 2.4 *Left panel* Polarization of a medium when a charge particle crosses it moving at a speed $v < c/n$. *Middle panel* Polarization of a medium when a charge particle crosses it moving at a speed $v > c/n$. *Right panel* Schematic view of the Cherenkov radiation emitted by the particle shown in the middle figure

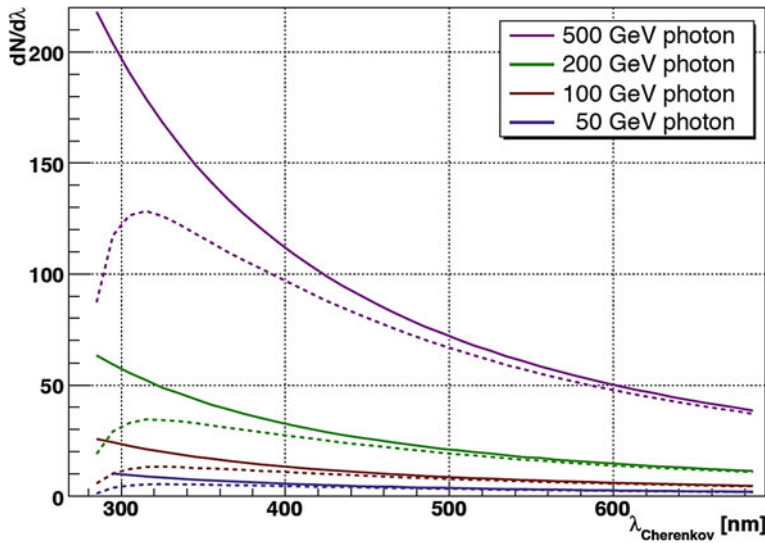
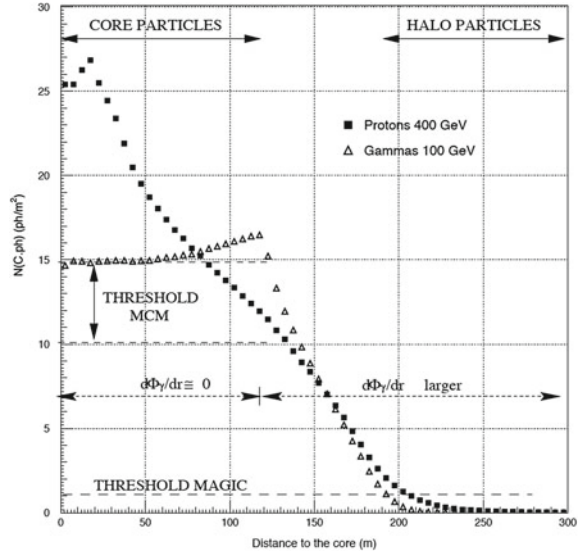


Fig. 2.5 Cherenkov light spectrum emitted for γ -ray showers of different energies. The *solid lines* correspond to the emitted spectrum at 10 km height and the *dashed ones* to that detected at 2200 m a.s.l.

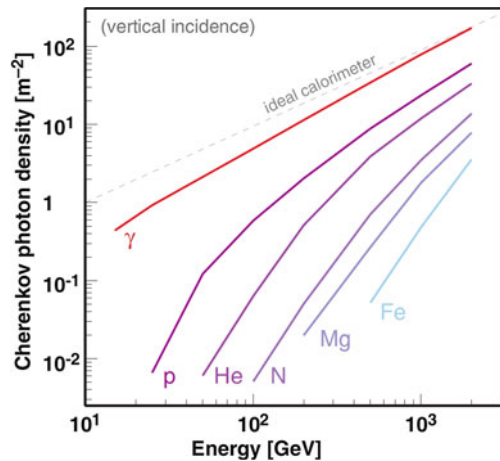
From Eq. 2.3 we see that the number of Cherenkov photons is inversely proportional to the square of their wavelength. From here it derives that most of the photons are emitted in the UV, as can be seen in Fig. 2.5. The observed spectrum is different from the emitted one due to several attenuation processes that occur in the particles track: Rayleigh scattering off air molecules ($\propto \lambda^{-4}$), that mainly affects the UV photons; Mie scattering off aerosols, water droplets and dust; UV absorption by ozone molecules; and infrared absorption due to H_2O and CO_2 . Due to all these processes, the maximum of Cherenkov light observed at 2200 m a.s.l. in a shower peaks at around 330 nm, independent on the energy of the incident particle (see Fig. 2.5).

Fig. 2.6 Lateral Cherenkov distribution density for a shower produced by a gamma ray of 100 GeV and a proton of 400 GeV. Taken from (Barrio et al. 1998)



For vertical incident gamma rays, the Cherenkov photon density is almost constant in a ring with radius $\lesssim 120\text{m}$ centered in the core of the shower as it is shown in Fig. 2.6. It is higher in the region known as the *hump* and then it fades away. The *hump* is produced by the increase in the angle θ due to a change in the refracting index of the atmosphere at different heights. The energy of an incident γ -ray photon is proportional to the Cherenkov photon density detected on the ground, fact used to reconstruct their energy. In the case of hadrons, this relation is not fulfilled, as can be seen in Fig. 2.7.

Fig. 2.7 Cherenkov photon density as a function of the energy for different incident particles (Wagner 2006; Oser et al. 2001)



2.1.3 The Imaging Technique

The main purpose of the imaging atmospheric Cherenkov technique is to combine the spatial and temporal information of the measured light to produce images of the showers and differentiate between hadron and γ -initiated showers. To achieve this, IACTs have large reflectors that collect the maximum amount of Cherenkov light from a single shower possible and pixelized cameras equipped with very fast response pixels. The events are triggered by systems that record them only when several pixels are above a certain threshold for a short time (the shorter the time, the less Night Sky Background (NSB) that is integrated). They are also equipped with fast readout systems to record and reconstruct the narrow signals the photodetectors issue when they are excited by photons.

The reflectors used are usually Davies-Cotton, that have a good off-axis performance, but are not isochronous. When the reflector size increases, the arrival timing difference to the camera plane of light reflected by different segments of the mirror becomes important and parabolic reflectors are used because they are isochronous, although they have large coma aberration for off-axis angles. The pixels are usually fast, high-Quantum Efficiency (QE) Photomultiplier Tubes (PMTs), although there have been recent developments on cameras using Silicon PhotoMultiplier (SiPM) showing a good performance (Bretz et al. 2014).

An scheme of how the technique works is shown in Fig. 2.8. The reason of using more than one telescope is to properly reconstruct the direction of the incident γ -ray and

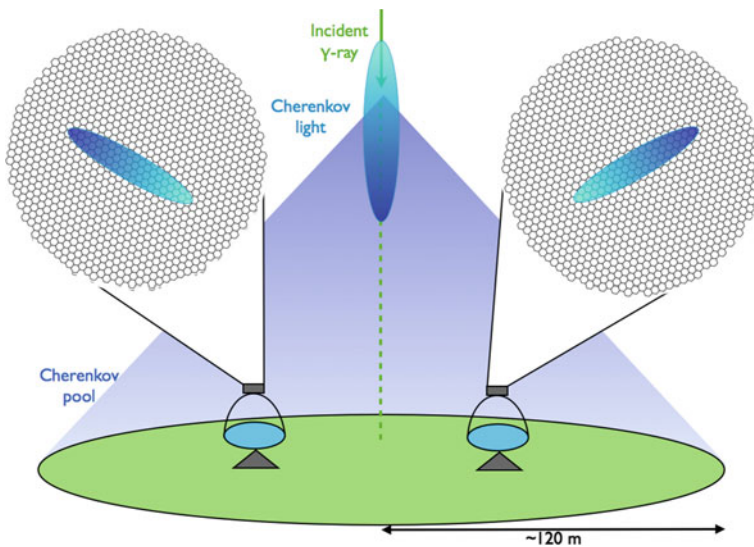


Fig. 2.8 Scheme of the imaging atmospheric Cherenkov technique

have a better background suppression. IACT systems usually work in stereoscopic mode, recording only the events triggered by more than two telescopes in a given time window.

Sources of background: Hadrons are arriving almost isotropically to the atmosphere, therefore the background contribution will come from everywhere. In fact, most of the events recorded by IACTs have hadronic origin (the proportion with respect gamma rays is $\sim 1000 : 1$ at 1 TeV for a strong source as Crab). The energy distribution of the hadronic background follows a power-law distribution $dN/dE \propto E^{-2.7}$. As it was described in the previous sections, the showers produced by primary particles of different origin have different shapes when projected in the camera (see Fig. 2.9). γ -ray showers produce elliptical images on the ground, while hadron-like cascades produce more irregular images. This fact is used at the analysis level to distinguish between EM showers and hadronic ones (see Sect. 2.2.3.3).

There are other sources of background, such as muons, that usually form ring-like images on the camera plane and can also be rejected because of their shape. On the other hand, there are also irreducible sources of isotropic background, such as cosmic e^\pm , that produce EM cascades identical to those produce by gamma rays, or diffuse gamma rays coming from the galactic plane as they were measured by Abramowski et al. (2014a).

Apart from Cherenkov photons, one has the contribution of the Night Sky Background (NSB), that are background photons propagating isotropically in the night sky. The NSB contribution in la Palma was measured to be $(1.75 \pm 0.4)10^{12} \text{ ph m}^{-2} \text{ sr}^{-1} \text{ s}^{-1}$ between 300 and 600 nm (Mirzoyan and Lorenz 1994).

Differences between observations at large Zenith distance (Zd): As some of the observations of this thesis were performed at high Zd (up to $Zd = 70^\circ$), we will give a brief description of the differences between the shower development and their

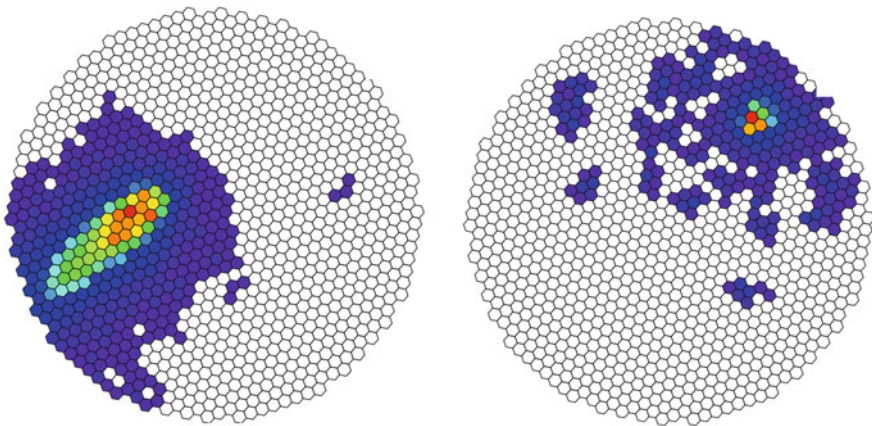


Fig. 2.9 Example of an image of a γ -ray (*left panel*) and hadron (*right panel*) showers

imaging at different Zd . When observing at high Zd , the shower development takes place in the upper layers of the atmosphere. This implies a larger path for the shower to go through the atmosphere, being approximately $L' \simeq L / \cos(Zd)$. The diameter of the plane perpendicular to the reflector follows the same relation $l' \simeq l / \cos(Zd)$. Since the amount of light reflected by the mirrors is proportional to the amount of light arriving to the plane perpendicular to the reflector, the photon density ρ arriving to the camera is proportional to the diameter square of the plane perpendicular to the reflector $\rho \propto l^2$ and the relation between the light density at high Zd ρ' and the one at $Zd = 0$ ρ is:

$$\rho' \propto l'^2 \propto \frac{\rho}{\cos^2(Zd)} \quad (2.4)$$

therefore larger attenuation and lower Cherenkov photon density at the observation level (see Fig. 2.10).

The reduction of Cherenkov light on the ground causes an increase in the energy threshold. It should theoretically increase with the Zd as $E_{\text{threshold}} \propto \cos^{-2}(Zd)$ due to the decrease in Cherenkov photon density, but is measured to increase faster with increasing Zd due to the worst imaging of the showers and the loss of discrimination power between the hadronic and EM ones. The worsening of the energy threshold is on the other hand compensated by an increase in the collection area of the telescope. As the Cherenkov light pool is larger when observing showers at high Zd , the collection area increases.

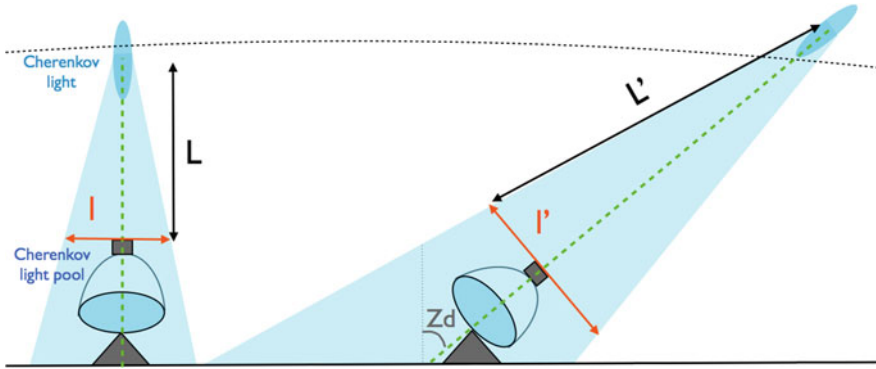


Fig. 2.10 Difference in the shower development between low Zd (left telescope) and high Zd (right telescope) observations. We can see that the distance from the camera to the point in the atmosphere where the showers start to develop is smaller for low Zd observation (L) than for high Zd observations (L'). The diameter of the Cherenkov light pool in the plane perpendicular to the reflector is also larger for high Zd observations ($l' \simeq l / \cos(Zd)$)

2.2 MAGIC

The Florian Goebel Major Atmospheric Gamma-ray Imaging Cherenkov (MAGIC) telescopes are a stereoscopic system of two 17 m diameter IACTs located on the Canary island of La Palma, Spain (28.8°N , 17.9°W at 2225 m a.s.l). The system is specially designed to achieved the lowest possible energy threshold and a fast response to transient phenomena. MAGIC I started to take scientific data in 2004 and MAGIC II in 2009 (see Fig. 2.11). During the summers of 2011 and 2012 the system underwent a major upgrade of the digital trigger, readout systems, and one of the cameras (Aleksić et al. 2014f) to make it homogenous and improve its performance. The MAGIC data analyzed in this thesis were taken both in stand-alone (only with MAGIC II) and stereo modes, hence both observation modes will be described.

2.2.1 Hardware Description

We will describe in the following the main components of the MAGIC telescopes. We will give a detailed description of the data acquisition and the electronic chain components relevant for data taking.



Fig. 2.11 Picture of the two MAGIC telescopes on the island of la Palma

2.2.1.1 Structure and Drive

The telescope mount is alt-azimuthal. The dish, moving in zenith and supporting the mirrors is identical in both telescopes and consists of a frame of octagonal shape made of carbon fibre-epoxy tubes joined by aluminum knots (see Fig. 2.12). The structure is rigid and light-weight (less than 20 tons including mirrors and camera support). The lower structure moving in Azimuth (Az) is made of steel tubes and weighs a total of 65 tons including the undercarriage (Fig. 2.12). To hold the camera, there is a aluminum circular tube anchored to the main structure by ten pairs of steel cables. The deformation of the structure is less than 3.5 mm for any of the telescope orientations (Bretz et al. 2009), which is corrected using the Active Mirror Control (AMC) described in Sect. 2.2.1.2.

The range of movement spans from -90 to 318° in Az and from -70 to 105° in Zd. There are two 11 kW motors in two of the six bogies composing the Az undercarriage and one motor of the same power for the zenith axis (see Fig. 2.12). The telescope's GRB mode allows to move 180° in 20 s. The telescope position is measured by three 14-bit shaft encoders, one of them in the Az axis and two in the zenith one. The telescope can track sources with an accuracy of 0.02° . To account of the deformation of the telescope structure, the pointing of the telescope is calibrated taking pictures of stars at different Zd and Az using a CCD camera installed in the middle of the reflector dish (*T-point* camera). In addition to the information given by the shaft encoders, the telescope pointing is constantly monitored by another CCD camera (*Starguider* camera), mounted in the center of the mirror dish as well. It measures the position of the telescope camera (with a ring of LEDs placed at the camera edge) respect to background stars and compares it to the latest available bending model (Fig. 2.13).

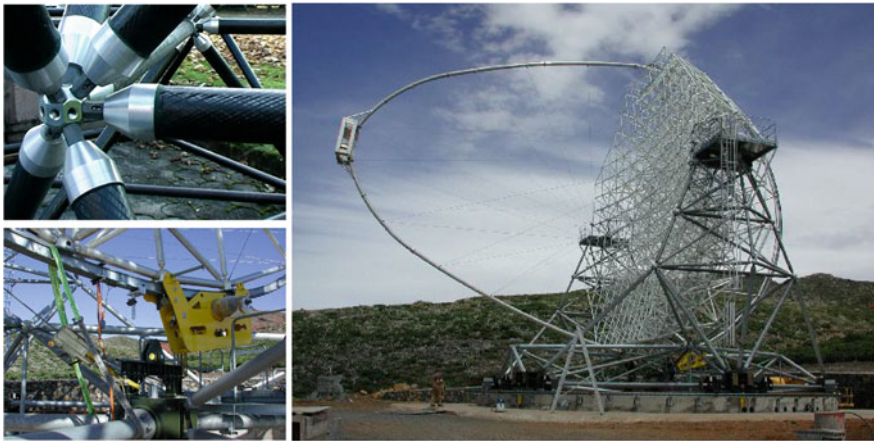


Fig. 2.12 *Top left* Aluminum knot where several carbon fibre-epoxy tubes join. *Bottom left* Zenith motor. *Right* Telescope mount without mirrors

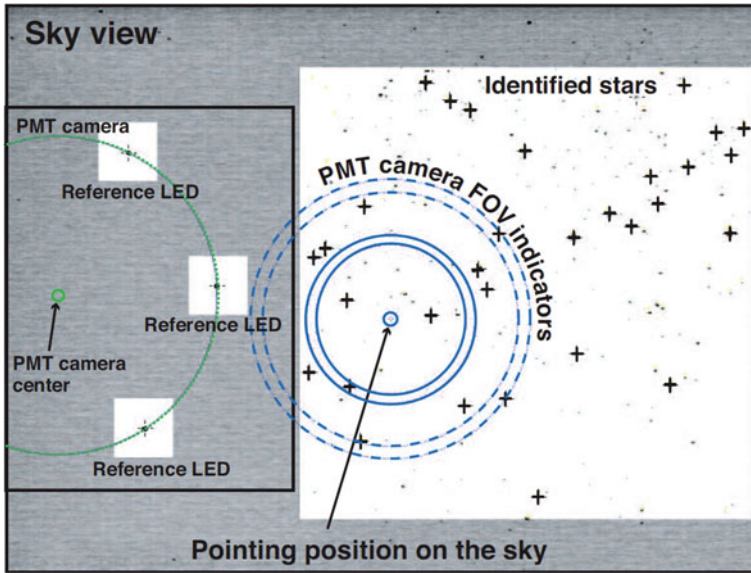


Fig. 2.13 Picture of the starguider camera installed in the central part of the MAGIC telescope. Taken from Wagner (2006)

2.2.1.2 Reflector and Mirrors

The reflector has $f = D = 17\text{ m}$, being f and D the focal length and diameter of the parabolic reflector dish. Parabolic mirrors are isochronous. As the time spread of Cherenkov signals is $1\text{--}2\text{ ns}$, Cherenkov pulses are not significantly broadened, the signal extraction time is reduced and less noise is integrated. The Point Spread Function (PSF) for each of the mirrors r_{39} , defined as the diameter of the camera that contains 39% of the light of a point-like source, is $r_{39} \sim 10\text{ mm}$ wide at the camera on-axis plane. Each of the mirrors has a spherical shape with radii ranging from 34 to 36.7 m to match the parabolic shape of the reflector. The total mirror surface of both telescopes is $\sim 236\text{ m}^2$. The reflective surface is tessellated with $1 \times 1\text{ m}$ facets (see Fig. 2.14a). In MAGIC I, each of the 247 facets contains four $0.5 \times 0.5\text{ m}$ aluminum honeycomb mirrors. In MAGIC II, there are 143 facets with single $1 \times 1\text{ m}$ all-aluminum mirrors on a honeycomb structure and 104 facets with single $1 \times 1\text{ m}$ glass-honeycomb-glass mirrors (see Fig. 2.14b). Each of the facets is controlled by the AMC software described in the following.

Active Mirror Control The AMC is the part of the hardware in charge of correcting mirror focusing depending on the Z_d for correcting for the deformations of the telescope. The system consists of two actuators per mirror panel. Each actuator can move the mirror with a precision of less than $20\text{ }\mu\text{m}$ corresponding to a shift in the camera plane of the light spot of less than 1 mm (Biland et al. 2008). The system adjusts the focusing of the mirror using Look-Up Tables (LUTs) binned in Z_d and

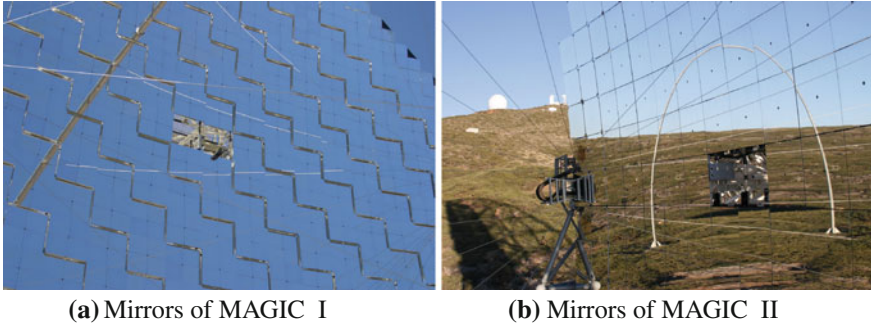


Fig. 2.14 MAGIC mirrors

Az. An optical PSF of $r_{39} \sim 11$ mm can be reached, very close to the theoretical minimum, which is the PSF of a single mirror. The AMC system also contains a high-sensitivity CCD camera called SBIG camera, used for measurements of the PSF of single and multiple-mirrors.

2.2.1.3 Camera

Each camera is one of the most important parts of the telescope. The cameras are made of high-QE PMTs (also known as pixels) to collect as much Cherenkov light as possible, fast response to integrate the minimum NSB possible and low gain to allow observing during moonlight conditions. Each of the PMTs is coupled to a light collector called *Winston cone* that increases the light collection efficiency and prevents the collection of photons coming with large angles with respect to the reflector, avoiding the collection of some light reflected by the ground and part of the isotropically distributed NSB. The first camera of MAGIC I had a different design as the current one, which is a clone of that installed in MAGIC II when it started operation. Since there were not data analyzed in this thesis with the old MAGIC I camera, we will only describe the current one.

The camera has a circular shape with ~ 1.2 m diameter and a weight of ~ 850 kg (see Fig. 2.15a). It has a Field of View (FoV) of 3.5° diameter and is composed of 1039 uniformly distributed PMTs. The camera also contains the power and cooling system, optical fibers and the electronics necessary to transmit signals to the *Counting House* (CH) where they are digitized. In front of the Winston cones there is a plexiglass window to protect the camera from the environment. To protect the camera from sun light and other external agents, it is equipped with movable lids.

PMTs PMTs are grouped in 169 clusters of 7 pixels, 127 of the clusters fully equipped and 42 (the outer ones) only partially. Each of the clusters is easily accessible from the back side of the camera for pixel exchanging (see Fig. 2.15b). Each PMT has a 0.1° FoV. The PMTs are Hamamatsu R10408 6-dynode photo-tubes with spherical photocathode and ~ 32 – 34% QE at 350 nm wavelength (Nakajima et al. 2013). Each

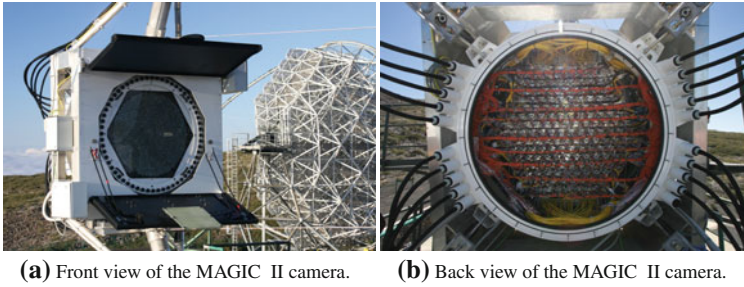


Fig. 2.15 MAGIC Camera

of the clusters is equipped with a slow control processor which controls several parameters of the PMT, as setting High Voltage (HV) or reading Direct Current (DC) currents. The HV is produced by a Cockroft-Walton type DC-DC converter. The PMT gain is $\sim 3 \times 10^4$ and the typical HV set is ~ 1250 V. After the PMT, the signal is further amplified by a low-noise pre-amplifier to account for the low gain of the PMT. The clusters are also equipped with a pulse generator that allows injecting signals to the pre-amplifier for testing purposes.

The analogue electronic signals are converted into optical signals by Vertical Cavity Surface Emitting Lasers (VCSELs) after the pre-amplifier stage. They are transmitted to the CH by 162 m long optical fibers.

2.2.1.4 Calibration System

To flat field the PMT gain, obtain the conversion factor between the counts of the digitizers to number of photoelectrons (phe) and the conversion between Flash Analog-to-Digital Converter (FADC) timing into an absolute timing, the MAGIC telescope needs a calibration system. It consists of a Nd-YAG laser, operating at 355 nm with 0.7 ns pulse width. To obtain a dynamic range, two rotating filter wheels can attenuate the laser beam, so that the signal produced in a PMT ranges between 1 and 1000 phe. To achieve an homogenous distribution of the calibration light at the camera plane, the laser beam is diffused using an integrating (Ulbricht) sphere. The system is placed in the center of the reflector dish.

2.2.1.5 Receivers

Trigger, readout electronics and Data AcQuisition (DAQ) are placed in a CH. We will describe the electronic chain that is followed by the signals coming from the telescope. The optical signals coming from the telescope through the optical fibers enter the so-called receiver boards where they are converted back to electric ones by photodiodes. The electric signals are then split into a trigger and a readout branch.

2.2.1.6 Trigger System

Digital trigger The current trigger system installed in the MAGIC telescopes for normal operation is a digital trigger composed of three stages (Paoletti et al. 2007):

- *Level 0 (L0)* trigger: Signals in the individual pixels go through discriminators with a given threshold. It is installed in the receiver boards and it issues a square signal of adjustable width every time the analog input of the telescope is over the Discriminator Threshold (DT).
- *Level 1 (L1)* trigger: It is a digital filter that searches for spatial and time coincidence of pixels that pass the L0 trigger. Pixels are grouped in 19 hexagonal overlapping cells called *macrocells*. Each hexagon is composed by 37 pixels, one of which is blind (see Fig. 2.16, left panel). When a pixel is above the threshold, an LVDS signal of 5.5 ns pulse is sent to the L1 board. If *n* Next Neighbour (NN) pixel signals overlap, the L1 issues a valid trigger. There are different NN multiplicities implemented in the L1 trigger ($n = 2, 3, 4$ or 5). The one currently used for stereo observations is $n = 3$, having an effective overlapping trigger gate of 8–9 ns. The NN configuration implies that the pixels above the threshold must be in a close compact configuration, being every pixel in the group in contact with at least other two (except for the 2NN configuration). The output signal of each of the 19 macrocells is processed by a Trigger Processing Unit (TPU) that merges them into an OR gate. The macrocells cover a region of $\sim 2.5^\circ$ diameter (Fig. 2.16, right panel).
- *Level 3 (L3)* trigger: It receives the output of the TPU from both telescopes and stretches it to achieve 100 ns width. It searches for an overlapping between the stretched signals of both telescopes in an effective time window of ~ 180 ns.

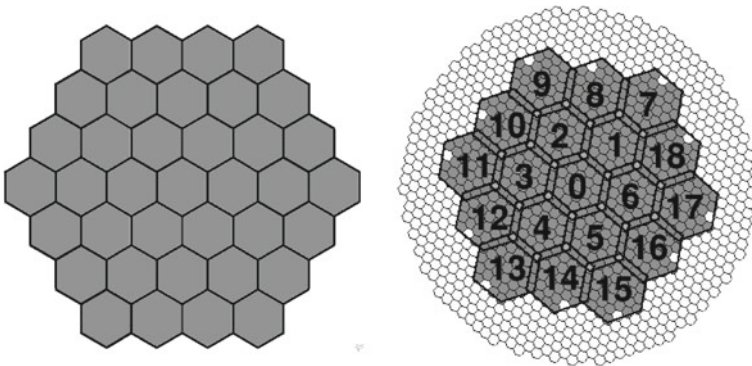


Fig. 2.16 The *left* figure is a picture of a single L1 macrocell, each of the hexagons corresponding to one pixel. The *right* one is the distribution of the L1 trigger macrocells in the MAGIC camera. The numbers are the ones used in the hardware identification of the macrocells. The lines are imaginary hexagons limiting each of the macrocells

Other trigger options MAGIC was designed to achieve the lowest possible energies. At the lowest energies, cosmic events are similar to “accidental” ones produced by noise. Several trigger options have been installed to discriminate accidentals from showers.

Sum trigger-II The Sum trigger-II is a trigger system based on the same concept as the Sum trigger designed for MAGIC I (Rissi et al. 2009), which allowed the discovery of VHE pulsed emission from the Crab pulsar above 25 GeV (Aliu et al. 2008). It adds up the analog signals from several pixels in 19-pixel macrocells. To minimize the effect of signals produced by After Pulses (APs) in the PMTs, the signal of every pixel is “clipped” before the analogue sum: if it exceeds a certain value, the analogue clipped signal that is sent to the adder is ideally constant. With the clipping of the signals, we avoid issuing valid triggers due to the signal coming from one or two pixels in the whole macrocell. The output of the adder enters a DT. The DT that is currently set in the MAGIC telescopes is of the order of several tens of phe to achieve the lowest possible energy threshold without exceeding the recording limit of the DAQ. For further information about Sum trigger-II, see (García et al. 2014).

Topo-trigger Special trigger option developed during this thesis that makes use of the digital macrocell information of both telescopes to record more low energy events. It has been simulated, tested and is currently under commissioning. A detailed description can be found in Chap. 4.

2.2.1.7 Readout

The readout is the part of the electronic chain that digitizes and temporarily stores the analogue signals from the telescope. We will briefly describe the history of the readouts used in MAGIC and then give a deeper explanation of the readout currently used, the Domino Ring Sampler (DRS) version 4.

Glimpse to the previous readouts used in MAGIC

Siegen: Between the beginning of MAGIC (~ 2003) and February 2007, MAGIC operated with a readout known as *Siegen*. The readout consisted of a dual gain 300 MSample/s system. Using this option, the readout system was too slow to handle the ~ 2 ns signals coming from the PMTs and they had to be stretched to 6–7 ns. Due to the stretching of the signals, the differences between signals produced by gamma rays, cosmic events or NSB were smoothed and the performance worse than with a faster readout. The dead time of the system was 25 μ s.

MUX: In February 2007, the MAGIC I readout was upgraded to a 2 GSAMPLE/s system which made use of a fiber-optic multiplexing technique (MUX). Multiplexing was possible thanks to the low duration of the signals (\sim few ns) and the trigger rate (it was typically ~ 1 kHz), resulting in a low duty-cycle for the digitizer. The system

was custom-made in order to reduce the cost and consumption and instead of using a FADC for each readout channel, a single FADC could handle 16 channels (Mirzoyan et al. 2002; Bartko et al. 2005). The dead time of the system was 25 μs .

DRS2 When MAGIC II was constructed, it was equipped with a readout based on the DRS2 analog memory chip. The working principle of the DRS is the following (see Fig. 2.17): the signal coming from the receiver board is sequentially connected to an array of 1024 capacitors by fast switches synchronized to an external clock. Each of the capacitors is charged by the analogue signal of the corresponding pixel for a time that is proportional to the period of the clock controlling the switching (the so-called Domino wave). The capacitors are overwritten after 1024 clock cycles. When a trigger is received, the Domino wave stops and the charge stored in the 1024 capacitors is digitized by an Analog-to-Digital Converter (ADC). Later on, only 80 capacitors are stored by the DAQ, but as the whole buffer needs to be read, the dead time of the system is 500 μs . This means that for a stereo trigger rate of $\sim 300\text{ Hz}$, the dead time is 15 %. DRS2 chips are highly non-linear and temperature dependent devices that need to be constantly calibrated. A complete description of the DRS2 chips can be found in (Bitossi 2009).

DRS4 To reduce the non-negligible dead time of the telescope using the DRS2 chip and to converge to one single readout in both telescopes, in December 2011 the MUX readout in MAGIC I and the DRS2 readout in MAGIC II were replaced by a readout based on the DRS4 chip. The DRS4 chip works basically like a DRS2 chip. They are still temperature dependent, so they still have to be calibrated on a regular basis, but they are linear and when a trigger is issued, only a Region of Interest (RoI) of 60 capacitors is read at 33 MHz, reducing the dead time to 27 μs . Additional

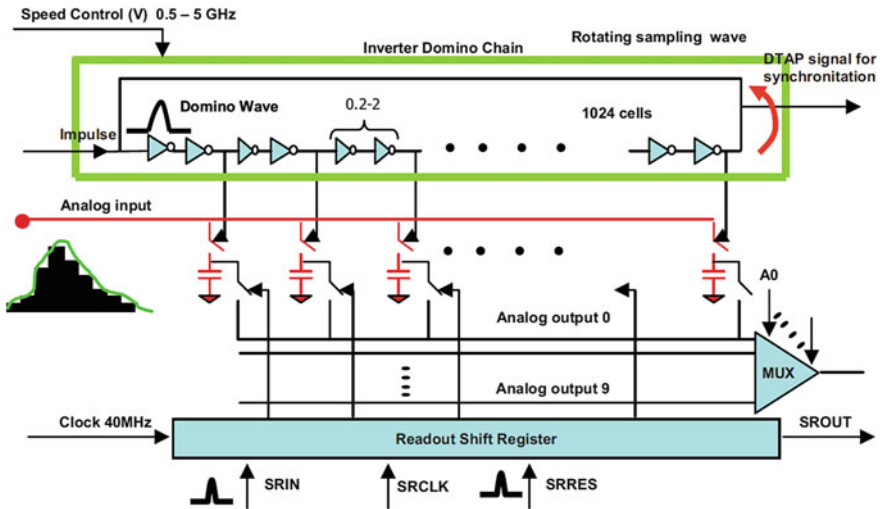
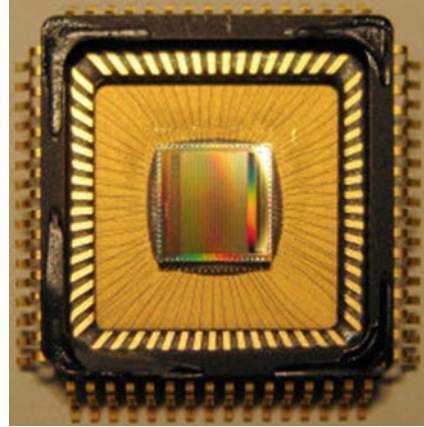


Fig. 2.17 Schematic view of the DRS chip. Taken from Bitossi (2009)

Fig. 2.18 Picture of the DRS4 chip currently used in the MAGIC telescopes



advantages with respect to the DRS2 chip are a larger bandwidth (700 MHz instead of 200 MHz) and a lower pedestal noise (0.7 phe per cell, a factor 2 lower). For a detailed characterization, see Sitarek et al. (2013) and for a picture of a DRS4 chip, see Fig. 2.18.

DRS chips are installed in especially designed boards called PULSer And Recorder (PULSAR). PULSAR boards are general purpose VME interface boards used in high energy physics. Each PULSAR board hosts 4 mezzanines, each mezzanine contains 3 chips and a single DRS4 chip has 8 channels, so every PULSAR board can digitize 96 pixels.

The data from the RoI of the DRS4 chip are read by the DAQ program. It interfaces with the PULSAR boards through FILAR cards and HOLA boards, which are respectively PCI cards installed in the DAQ computer and mezzanines installed in the PULSAR boards. The signal is transmitted from the HOLA to the FILAR boards via optical S-Link. The DAQ program then runs three threads in parallel: reading, analyzing and storing. There are 14 PULSAR boards to digitize all the pixels in a telescope, and there are two additional PULSAR boards with special functionalities: the “digital PULSAR” that adds digital information to the data such as trigger number and absolute time, and the “busy PULSAR”, which stops the triggers when the system is processing an event or an error occurs (Tescaro et al. 2009, 2013).

Rate limiter: The current DAQ can handle a short-term event rate up to 3 kHz. When the telescope was illuminated by car flashes, or what is more important, when bright stars suddenly entered in the FoV while repositioning to a GRB, the DAQ crashed due to the very high stereo rate. It takes several minutes to recover from such a crash. A “rate limiter” was installed to momentarily block triggers when the rate exceeds 1 kHz.

2.2.1.8 Other Subsystems

Timing system The absolute time is generated by a Rubidium clock with a precision of 3×10^{-11} in 1 second. The Rubidium clock is a high-precision system, however it drifts over long time scales. To correct it, the device is synchronized every second to a GPS signal with a precision of the order of nanoseconds. The absolute time enters the data stream through the PULSAR.

Central pixel The central pixel of both MAGIC cameras is a modified PMT designed to detect variations of the optical flux of rapid-variability sources such as pulsars (Lucarelli et al. 2008). The pixel has a modified DC branch and a dedicated readout. The whole central cluster of the MAGIC camera was modified to host the necessary additional electronics, so it can be used for regular and optical observations.

Weather station A Reinhardt MWS 5 MW weather station is installed on the roof of the CH of the MAGIC telescope. It measures the temperature, pressure, humidity and wind speed and direction every second to determine if atmospheric conditions allow observations. For the atmospheric safety limits see Sect. 2.2.2.2.

Light Detection And Ranging (LIDAR) An elastic single-wavelength LIDAR is installed in the dome of the CH (Fruck et al. 2014). The LIDAR is equipped with a 5 mW Q-switched, pulsed Nd:YAG laser with a 532 nm wavelength, a 60 cm diameter, 1.5 m focal length Al mirror, a robotic equatorial mount, an Hybrid Photo Detector (HPD) capable of single photon counting and a computer equipped with an FADC card which digitizes the output of the HPD. The LIDAR operates as follows: it sends light pulses up to the atmosphere and they are backscattered by clouds or aerosols. The arrival time distribution of the backscattered photons registered at the HPD can be used to measure the transparency of the atmosphere.

Pyrometer The pyrometer is a device that computes the transparency of the atmosphere by measuring the temperature of the sky. It is installed in the MAGIC I reflector and points parallel to the telescope. It measures IR radiation in the 8–14 μm range and fits it to a blackbody spectrum. If the sky is cloudy, it reflects thermal radiation from the Earth and the sky temperature is higher. This temperature is used to determine a parameter known as *cloudiness*, that gives an estimate of the transparency of the atmosphere. It is defined as:

$$\frac{T_{\text{low}} - T_{\text{meas.}}}{T_{\text{low}} - T_{\text{up}}} \quad (2.5)$$

where $T_{\text{meas.}}$ is the measured temperature of the sky, $T_{\text{up}} = 200 \text{ K}$ corresponds to the best condition of the sky and $T_{\text{low}} = 250 \text{ K}$ to the worst.

AllSky camera The AllSky camera is a monochrome AllSky-340 camera manufactured by SBIG. It points to the zenith and has a FoV of 360° in Az and almost 90° in Zd. It takes an image of the sky every 2 min, with an automatically adjusted exposure time. The images taken by the camera are automatically uploaded to a server and can be monitored online.

MAGIC OnLine Analysis (MOLA) MOLA is a multithreaded C++ program used to obtain on-the-flight estimations on the γ -ray emission from sources in the FoV observed by MAGIC (Tescaro et al. 2013). It runs three parallel threads: two reading threads used to gather the single-telescope charge and arrival time of the events and an analysis thread that matches and reconstruct the events from the two telescopes. It computes the θ^2 plot with respect to the candidate source position and it also produces light curves of the measured γ -ray flux and skymaps. The program is specially used for nightly estimations on the flux of variable γ -ray sources such as blazars. Its most remarkable achievement was the discovery of a very rapid flare on the IC 310 galaxy while observing NGC 1275 and the extension of those observations (Aleksić et al. 2014a).

GRB monitoring alert system A GRB monitoring program runs in the background of one of the CH computers. It receives information of the GRB from the GRB Coordinate Network (GCN) and evaluates the observability of the received alerts following several criteria (distance to the Sun and to the Moon, Z_d, uncertainty on the position). If the alert fulfills all the criteria, the Central Control (CC) takes control of the observation and automatically points the telescope to the GRB location.

2.2.2 Data Taking

MAGIC standard operation and under which it achieves its best performance is under so-called “dark conditions” (i.e. when the moon absent from the sky). The total amount of available *dark* time amounts to ~ 1600 h/yr. About $\sim 65\%$ of the available dark time is observed and the rest is loss due to bad weather or technical problems. Thanks to the low gain of the PMTs, MAGIC can also observe during moonlight conditions up to 75 % of the moon phase and only has to stop observations on the 3 to 4 full-moon nights. Filters for moonlight observations (see Fig. 2.19) similar to those currently being used by VERITAS (Staszak 2014), are currently being commissioned and will allow the extension of the observations to any moon phase.

The default data taking mode of MAGIC is the stereo mode. The mean L0 DT is set to ~ 4.5 phe in both telescopes (slightly higher in MAGIC II due to the higher mirror reflectivity), although the individual pixel DT is controlled by means of an Individual Pixel Rate Control (IPRC). It sets the DT of individual pixels and controls that the L0 rate is contained within the limits established. Currently, for *dark* observations, the usual L0 rate is ~ 800 kHz. The IPRC decreases the L0 DT when the rate is lower than 250 kHz and increases it when the rate is larger than 1.2 MHz. For *moon* observations, the usual L0 rate is ~ 500 kHz, the DTs are decreased when the L0 rate is lower than 150 kHz and they are increased when the L0 rate is larger than 700 kHz. The L1 rates for standard operation are ~ 15 kHz in both telescopes, leading to an accidental stereo rate of 40 Hz (the calculation of the stereo accidental rate is explained in Sect. 4.1). During the operation and to ensure a correct calibration of the readout, there are

Fig. 2.19 Filter for moonlight observations



also 25 Hz of interleaved calibration events and 25 Hz of interleaved pedestal events recorded. The L3 stereo rate recorded by the DAQ is 250–350 Hz, so the current cosmic rate recorded is between 200–300 Hz.

The CC of the telescope, called SuperArehucas, takes care of all the subsystems of the telescope. It sends and receives reports with the state of all the hardware subsystems every second and allows the observers to control their most important functionalities. A detailed description of the CC program can be found in Zanin (2011).

2.2.2.1 Pointing Modes

The MAGIC telescope takes data in two different pointing modes: the *ON/OFF* and the *wobble* modes:

- *ON/OFF*: In the ON/OFF mode, the position of the target is tracked at the center of the camera. Two different types of observations have to be performed: *ON* observations with the source in the center of the camera, and *OFF* observations, preferably under similar Z_d/A_z conditions on a region where no γ -ray emission is expected.
- *Wobble*: This pointing mode was first proposed by Fomin et al. (1994) and it consists on tracking alternative positions in the sky that are at a slight offset from the center of the camera. For MAGIC the usual offset is 0.4° and each position is observed during 20 min. It has the advantage that no dedicated OFF observations have to be performed because the OFF is taken simultaneously. If only one OFF position is selected, it is taken in the opposite position of the camera with respect to the camera center as it is shown in Fig. 2.20a. More than one simultaneous OFF positions are possible, as can be seen in Fig. 2.20b. The collection of more

background events allows increasing the significance due to the more precise background determination. In addition, the background is evaluated from the same data sample as the signal, hence it matches its Z_d/A_z distribution and background light conditions. The main drawbacks from this observation mode are: a loss on γ -ray efficiency of the order of 15–20% because the source is 0.4° from the center of the camera and a systematic uncertainty in the background determination due to the camera inhomogeneities. These inhomogeneities are caused by dead pixels in the camera, non-flat trigger efficiency in the whole camera and insufficient flat fielding of the camera due to the gain differences between PMTs.

Independent of the pointing mode, working in stereoscopic mode makes the telescope acceptance dependent on the relative pointing of the telescopes. Only the events triggering both telescopes are recorded, therefore there will be more recorded events from the showers developed between the two telescopes and this is what is called the *stereo blob*. This problem was partially solved after the upgrade, when the system was homogenized and the trigger regions made equivalent. Currently, most of the observations carried out with MAGIC are in *wobble* mode.

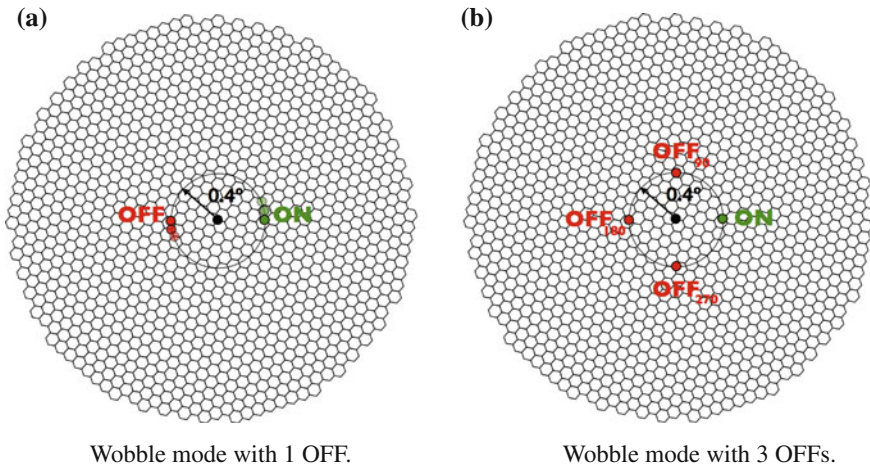


Fig. 2.20 Schematic view of the *wobble* pointing mode. The *black circle* marks the center of the camera. A region placed 0.4° from the source is tracked, being the source all the time situated at this distance from the center of the camera (*green circle*). The simultaneous background is taken all the moment from a region situated in the opposite side of the circle with center in the center of the camera and radius 0.4° (*red circle* in the *left* figure) in the case of 1 OFF region. In the case of 3 or more OFF regions, the background is taken from regions separated the same distance from one another in the aforementioned circle as it is shown in the *right* figure. The subindex of the OFF regions determine the angle turned in the circle counted counterclockwise from the ON region

2.2.2.2 Safety Limits

There are several atmospheric or technical conditions under which the telescope cannot be operated without taking the risk of seriously damage it. Here are the safety limits that should be fulfilled:

- Wind gusts < 40 km/h
- Wind mean speed < 50 km/h
- Humidity $< 90\%$
- Average PMT current $< 30\mu\text{A}$
- Individual PMT current $< 47\mu\text{A}$
- $Z_d > 1.5^\circ$

2.2.2.3 Data Types

There are different data types that can be taken with MAGIC. In the following, we find a summary of the most common ones that have to be taken every night:

- **Pedestal subtraction run (B):** Taken at the beginning of the night to calibrate the baseline of the DRS capacitors and set the zero level to 10000 counts to avoid problems with negative values due to the noise fluctuations. It has to be taken at least one hour after the electronic was switched on because of the temperature dependency of the DRS chips.
- **Pedestal run (P):** It records randomly triggered events (usually 2000 per run) which contain only noise. It has to be taken with the camera open to evaluate the effect of the NSB and readout noise to calculate the pedestal offset to be subtracted in the calibration of the data.
- **Calibration run (C):** It contains events triggered by the calibration system. They are later used in the analysis to calibrate the data.
- **Data run (D):** It contains all the events that issued valid triggers from the telescopes. They are mainly cosmic events, although it also contains interleaved calibration and pedestal events, together with accidental events triggered by noise. They correspond to approximately 20 min of data taking, the time that one wobble lasts. Data runs are divided into subruns which contain ~ 1 Gb of data, corresponding to ~ 2 min of data.

2.2.3 Data Analysis

The standard software for MAGIC data analysis is called MAGIC Analysis and Reconstruction Software (MARS) (Zanin et al. 2013). It converts the raw ADC counts recorded by the DAQ into high-level products using a collection of programs

written in C++ language that makes use of ROOT¹ libraries. The final purpose of the software is to reconstruct the primary particle generating the cascade and determine the direction and energy of the γ -ray candidates. In the following there is a summary of the processes performed by MARS:

- *Calibrate* the digital signals contained in the raw data and convert the information to phe (Sect. 2.2.3.2).
- *Image cleaning* and calculation of the *image parameters* for single-telescope (Sect. 2.2.3.3).
- *Merge* the data from both telescopes and calculate the *stereo image parameters* (Sect. 2.2.3.5).
- *Train* Random Forest (RF) for γ /hadron separation, fill LUTs for energy reconstruction and reconstruct the shower direction (Sect. 2.2.3.6).
- *Apply* RFs and LUTs to the data to calculate the *hadronness*, reconstructed energy and arrival direction of each event (Sect. 2.2.3.6).
- Calculate *signal significance* (Sect. 2.2.3.7), *skymaps* (Sect. 2.2.3.8), *spectra* and *light curves* (Sect. 2.2.3.9).

A scheme of the aforementioned process followed by the data is shown in Fig. 2.21. We will give a detailed description of the programs in the following sections.

2.2.3.1 Monte Carlo Simulation

As IACTs cannot be calibrated with a source of gamma rays, one has to trust on simulations to reconstruct the energy and incoming direction of the events. The Monte Carlo (MC) simulation is performed outside the MARS framework and is composed of three stages (for further information, see Majumdar et al. (2005)):

- The *atmospheric simulation* is performed using the Corsika 6.019 program (Heck et al. 1998), which simulates air showers. As an atmospheric model, we have used the so-called “MagicWinter” containing a mixture of N₂ (78.1 %), O₂ (21.0 %) and Ar (0.9 %). The model to describe hadronic interactions is FLUKA, together with the QGSJet-II model for high-energy interactions. Electromagnetic interactions are simulated using the EGS4 model. MAGIC simulations work with a modified version of CORSIKA that stores the information of the direction and position in the ground of the Cherenkov photons produced in the shower.
- The simulation of the telescope’s *mirror response* to the incoming Cherenkov light and its absorption in the atmosphere, is done by the *reflector* program. It uses the Elterman model for the aerosol distribution in the atmosphere (Elterman 1964). It simulates the absorption of Cherenkov photons in the atmosphere and their reflection in the telescope’s dish and calculates their position and arrival time at the camera plane.

¹<http://root.cern.ch/drupal/>.

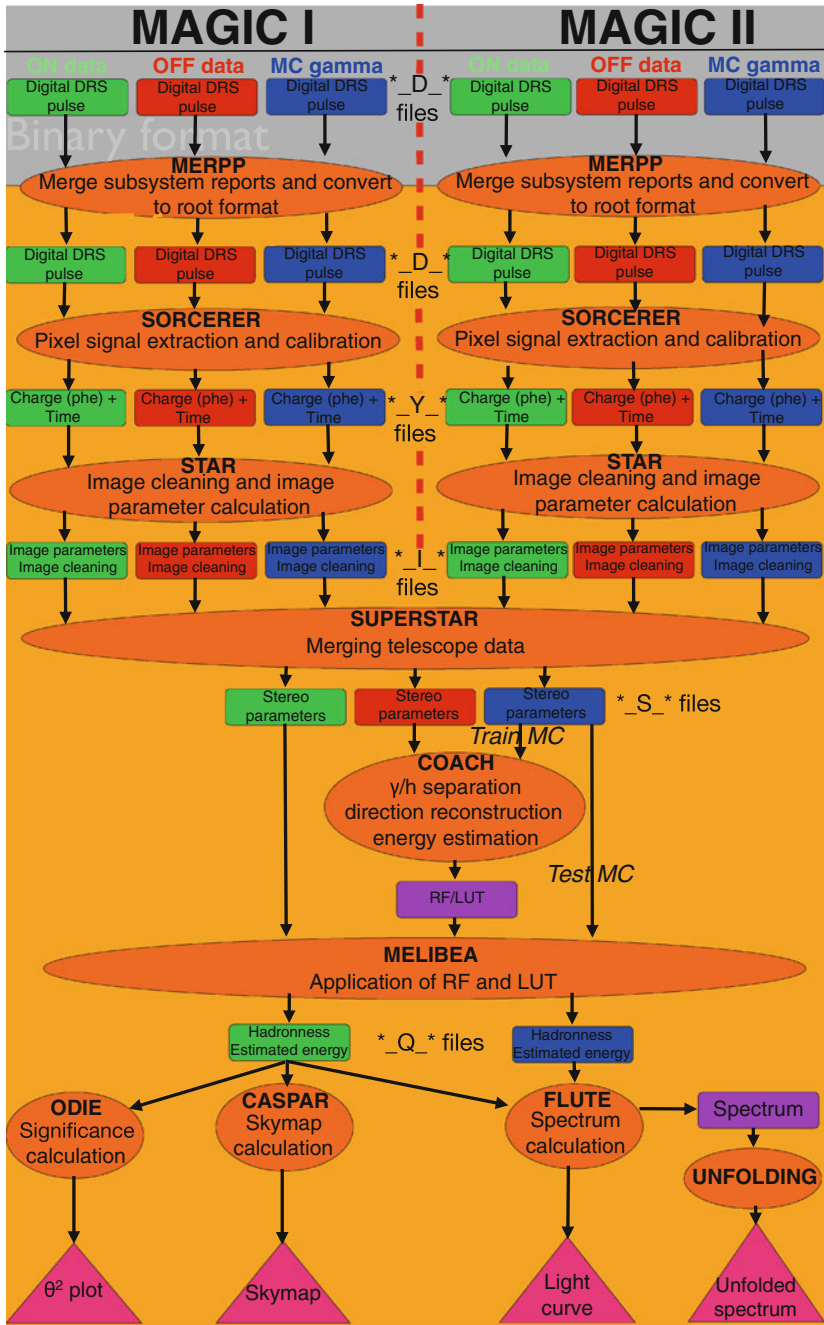


Fig. 2.21 Scheme of the MAGIC analysis chain

- The response of the PMTs and the readout electronics are simulated using the camera program. The measured QE of the PMTs is taken into account to simulate the pixel response, the trigger is simulated and the measured readout noise is also included in the simulation. The program also simulates the effect of the measured PSF of the individual mirror facets and their error in the alignment.

Recently, a new simulation program integrated in the MARS framework that simulates the reflector and camera response called *matelsim* has been developed (López 2013). However this program is still under testing and the official MAGIC simulation programs are still *reflector* and *camera*.

The output of the camera program has the same format as the raw data after converting it to ROOT data format, so it can be analyzed using the same software. For data analysis, only simulations of gamma rays are necessary, however one can also simulate with CORSIKA several types of particles and in MAGIC also e^\pm , p and He^{++} are used for performance studies. For most of the sources, gamma rays are simulated in a ring of 0.4° radius centered in the camera center (known as *ringwobble* MC, see Fig. 2.22a). However, for the analysis of extended sources or sources situated at different off-axis angles, *diffuse* gamma rays are simulated in a circle with radius 1.5° centered in the center of the camera (see Fig. 2.22b). MC gamma rays are produced in ranges of Z_d : low ($5-35^\circ$), medium ($35-50^\circ$), high ($50-62^\circ$) and very-high ($62-70^\circ$) Z_d . The distribution of generated MC gamma rays is flat in $\cos(Z_d)$ in each of the ranges. The ranges are selected to have similar coverage in $\cos(Z_d)$ in all bins.

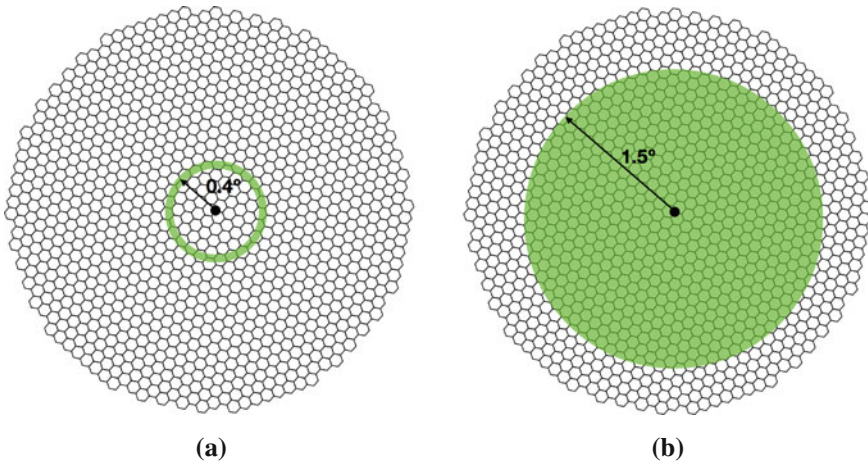


Fig. 2.22 Ringwobble (*left panel*) and diffuse (*right panel*) MC schemes. The *green* shaded area is the one where the MC gamma rays are simulated

2.2.3.2 Signal Extraction and Calibration

The raw data, with the output of the digitizers in counts vs time is converted to ROOT format by a program called `merpp` (MERging and Preprocessing Program) which also merges the data file and the subsystem reports.

Once the data is in ROOT format, it can be calibrated to convert ADC counts into number of phe. The old calibration program was called `callisto` (CALibrate LIght Signals and Time Offsets), but after the installation of the DRS4 readout in both telescopes, a new program called `sorcerer` (Simple, Outright Raw Calibration; Easy, Reliable Extraction Routines) was developed to handle DRS-related problems. 60 “time slices” are stored for each pixel, corresponding to 60 capacitors, each of them containing the number of ADC counts in 0.5 ns). The pedestal subtracted from each time slice depends not only on the capacitor that is read, but also on the last time it was read. After the pedestal is subtracted, the *sliding window* algorithm is used to extract the signal. It takes the maximum resulting from integrating 6 consecutive slices. The signal arrival time is the average position of the selected 6 slices weighed with the ADC counts contained in each of them.

The conversion from ADC counts to number of phe is performed using the *F-factor* method (Mirzoyan 1997). For calibration pulses it is assumed that the number of phe follows a Poissonian distribution with mean N and standard deviation \sqrt{N} . The distribution of measured charge in ADC counts Q has a mean $\langle Q \rangle$ and a deviation σ_Q which is wider than pure Poissonian expectations due to noise in the PMT e^- multiplication process. The relative amplitude of both distributions can be written as follows:

$$F \frac{\sqrt{N}}{N} = \frac{\sigma_Q}{\langle Q \rangle} \quad (2.6)$$

where F is the so-called *F-factor*, which is different for each PMT and must be measured in the laboratory. The electronic chain also contributes to the broadening of the peaks, but this contribution is negligible with respect to the effect of the PMT. Since the spread of *F-factor* for the PMTs of each telescope is small, one can take one single *F-factor* for each of the telescopes. The conversion factor m between ADC counts and phe is then given by:

$$m = \frac{N}{\langle Q \rangle} = F^2 \frac{\langle Q \rangle}{\sigma_Q^2} \quad (2.7)$$

As the gain of the VCSELs is not constant in time, m must be updated using calibration events interleaved with cosmic events at a rate of 25 Hz.

2.2.3.3 Image Parameter Calculation and Image Cleaning

From this step on, the shower images are parametrized and the pixel information is lost. The program performing all these computations is called `star`. The charge and

arrival time information are used for the analysis and only pixels that contain useful information about the shower are kept for the shower parametrization (see Fig. 2.23). The algorithm to remove the noisy pixels is called *image cleaning* (Aliu et al. 2009; Lombardi 2011).

In the *absolute* image cleaning method, a pixel is considered a “core pixel” if its charge is above a certain threshold Q_c , if it is adjacent to another core pixel and if its arrival time does not differ from the mean arrival time of the core of the image by more than Δt_c . Boundary pixels are defined as the ones above a threshold Q_b , that are adjacent to at least one *core* pixel and if their arrival time does not differ from the arrival time of that *core* pixel a time larger than Δt_b .

For the single-telescope data used in the analysis of Chap. 9, the values used to define *core* and *boundary* pixels are the following:

$$Q_c = 8 \text{ phe}; \quad Q_b = 4 \text{ phe}$$

$$\Delta t_c = 4.5 \text{ ns}; \quad \Delta t_b = 1.5 \text{ ns}$$

In the *sum* image cleaning method, the algorithm searches for 2, 3 or 4 neighboring pixels (2NN, 3NN, 4NN) with a summed charge above a certain threshold Q_c in a time window t_c . To prevent from large signals due to APs, each pixel’s signal is clipped before the sum. The threshold values and the time windows applied to search for *core* pixels with the *sum* algorithm can be found in Table 2.1. Once the *core* pixels are selected, the *boundary* ones are the ones at least neighbour to one *core* pixel, their charge is larger than 3.5 phe and their arrival time difference with respect to their *core* neighbour pixel is smaller than 1.5 ns.

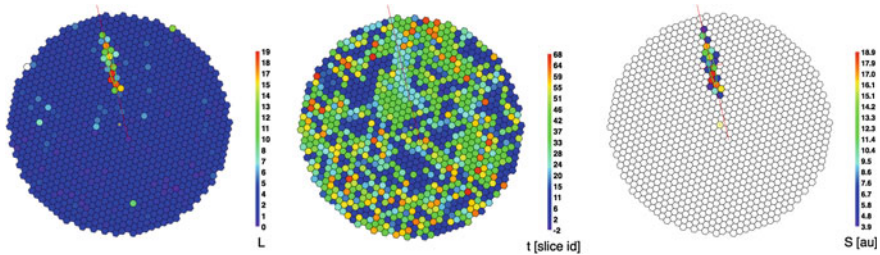


Fig. 2.23 Signal charge (*left panel*), arrival times (*middle panel*) and cleaned image (*right panel*)

Table 2.1 *Sum* cleaning charge and time parameters

Topology	Q_c [phe]	t_c [ns]
2NN	2×10.8	0.5
3NN	3×7.8	0.7
4NN	4×6	1.1

Once the *core* and boundary pixels are selected, the resulting images are parametrized and this is the information that is stored in the data. The image parameters used in the MAGIC analysis are the following:

Hillas parameters An ellipse is fit to the pixels after cleaning. The momenta of this fit up to second order are used to parametrize the image (Hillas 1985):

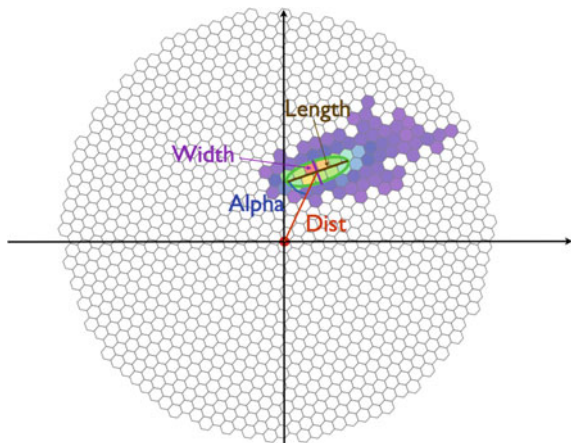
- **Size:** Total charge (in phe) contained in the image. It is related to the energy of the primary γ -ray if the shower falls close to the telescope (usually $\lesssim 120$ m).
- **Width:** RMS spread along the minor axis of the ellipse fitting the image. It is a measurement of the lateral development of the shower.
- **Length:** RMS spread along the major axis of the ellipse fitting the image. It is a measurement of the longitudinal development of the shower.
- **Center of Gravity (CoG):** Center of gravity of the image. It is computed as the mean of the X and Y weighted mean signal along the camera coordinates.
- **Conc(N):** Fraction of the image concentrated in the N brightest pixels. It measures how compact the shower is and tends to be larger in gamma rays.

A shower image with some of the *Hillas parameters* can be seen in Fig. 2.24.

Source-dependent parameters: They are still related to the physical properties of the shower, but they depend on the expected position of the source.

- **Dist:** Angular distance from the source expected position in the camera to the CoG of the shower image. This parameter is larger for the showers with larger impact parameter.
- **Alpha:** Angle between the ellipse major axis and the line connecting the expected source position to the CoG of the shower image. As the showers produced by gamma rays coming from the shower should point to the source position in the camera, this angle is small for γ -like showers.

Fig. 2.24 Picture showing some of the *Hillas parameters*



Time parameters: Since γ -like events are shorter in time than hadron-like events, time information is also useful to discriminate between hadron and γ -induced showers.

- **Time RMS:** RMS of the arrival times of the pixel that survived the *image cleaning*. It is smaller for γ -like showers.
- **Time gradient:** Slope of the linear fit to the arrival time projection along the major axis of the ellipse. It measures the direction of the shower development, positive if coming to the expected source position and negative otherwise.

Image quality parameters: They are used to evaluate if the image is very noisy or if it is well contained in the camera.

- **LeakageN:** Fraction of the size of the source contained in the N outermost rings of the camera.
- **Number of islands:** Number of non-connected pixels that survived the image cleaning.

Directional parameters: They discriminate between the head (top part of the shower) and tail (bottom part of the shower). Typical showers have higher charge concentration in the head than in the tail.

- **Asymmetry:** Signed distance between the shower's CoG and the pixel with the highest charge. It is positive when the pixel with the highest charge is closer to the camera center than the CoG.
- **M3Long:** Third moment of the shower image along its major axis. It follows the same sign criterium as the Asymmetry parameter.

2.2.3.4 Data Quality Selection

Data affected by technical problems, bad weather or different light conditions (e.g. data taken under moonlight conditions) should be separated from the “good” dataset. Some of this data could be recovered, follow a parallel analysis and their final products merged with those of the “good” dataset, although most of the times they are rejected.

To distinguish between good and bad quality data, we use several indicators. We plot the number of visible stars the starguider detect and the average *cloudiness* for every subrun. If the *cloudiness* is above 40, the data is considered of bad quality. We also plot the *rate* above a low *size* cut (usually 50 phe). This allows to reject accidental events and plot the real cosmic rate. This rate is different depending on the Z_d . We can empirically correct the rate multiplying it by $\cos^{-1}(Z_d)$. For a dark night with good weather conditions, the cosmic rate corrected by the Z_d is constant. This empirical correction is valid up to $Z_d \sim 50^\circ$. For the same observation period and for each telescope, where we expect a similar rate for good quality nights, we calculate the average cosmic rate and we accept data with a rate within 15 % of the average rate. The subruns outside this range might be affected by atmospheric extinction or technical problems and are rejected. The average rate is different for

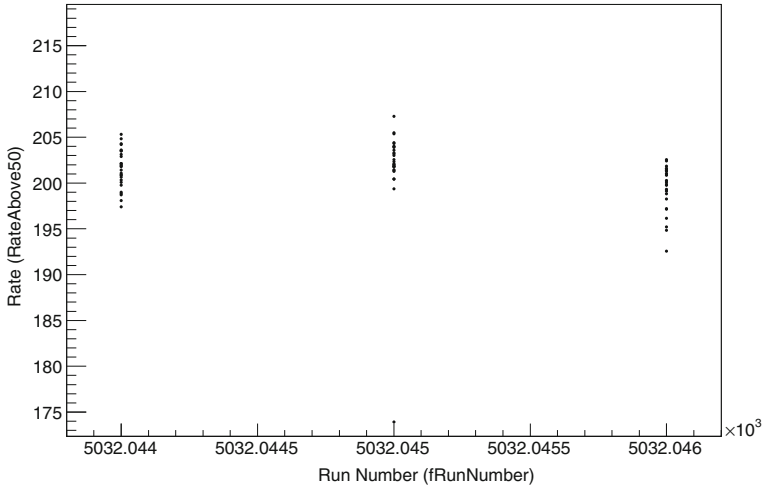


Fig. 2.25 Rate plot for the data quality selection for MAGIC I rate (for $size > 50$ phe) is plotted as a function of run number. Each of the points corresponds to the rate of a 2-min subrun

each of the telescopes: MAGIC II rate is usually higher than MAGIC I due to the higher reflectivity of the mirrors installed in MAGIC II. A plot where a typical data quality rate plot is shown in Fig. 2.25.

2.2.3.5 Stereo Image Parameter Calculation

Once good-quality data have been selected, the `superstar` program merges the two telescopes data. One can now reconstruct the three-dimensional shower development and determine several parameters useful for the energy and direction reconstruction. Some of them are shown in Fig. 2.26a.

- **Impact point:** The impact point on the ground is calculated using the crossing point of the major axis of the two shower images and the position of each telescope (see Fig. 2.26b).
- **Shower axis:** The shower axis is given by the crossing point of the major axis of the two superimposed shower images in the camera plane, as can be seen in Fig. 2.26c. This is the so-called *crossing point* method to calculate the shower direction (Aharonian et al. 1997b; Hofmann et al. 1999). The more powerful *disp* method will be described in Sect. 2.2.3.6.
- **Height of shower maximum:** Using the shower axis, together with the angle at which the CoG of the image is measured with respect to each telescope, one can estimate the height of the shower maximum (H_{\max}). The H_{\max} is in inverse proportion to the energy, as it was shown in Sect. 2.1.1.1. This parameter is strongly correlated with the shower energy and is a powerful γ /hadron discriminator.

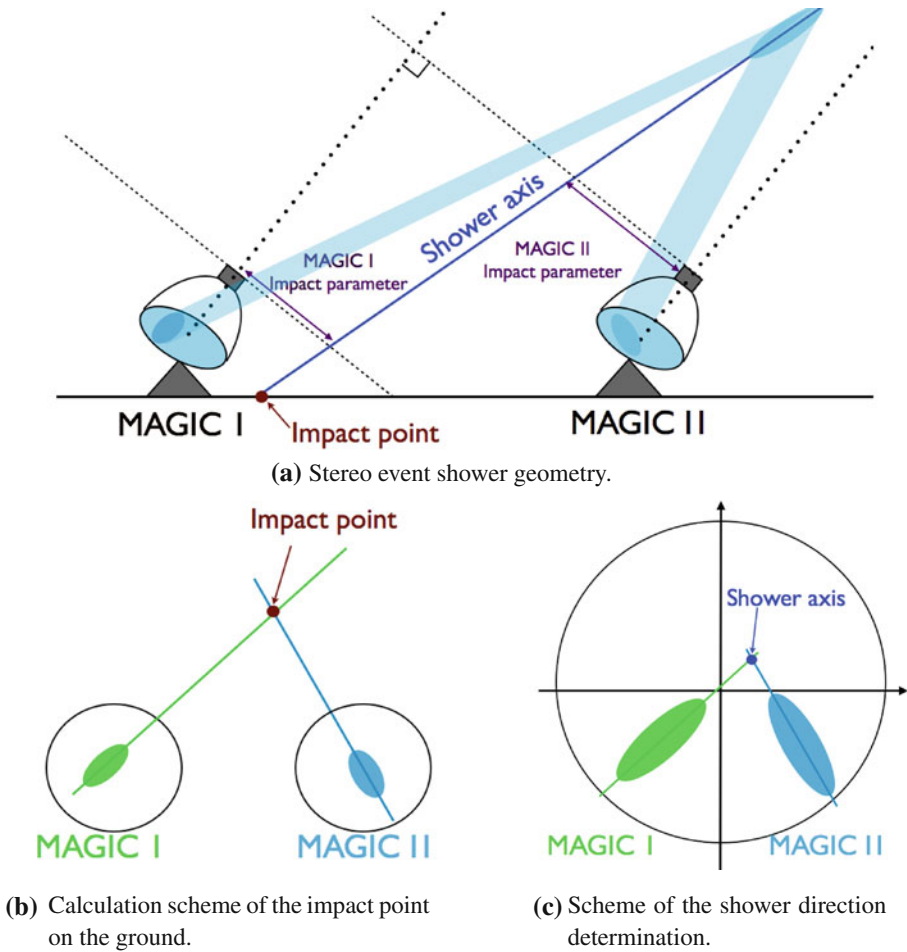


Fig. 2.26 Different views of the shower geometry

- **Impact parameter:** Calculated as the perpendicular distance between the shower axis and the pointing direction of each telescope.
- **Cherenkov radius:** It is computed as the radius of the ring of Cherenkov light pool produced by an e^- with the critical energy of 86 MeV at the height of shower maximum.
- **Cherenkov photon density:** Cherenkov photon density on the ground of a shower produced by an e^- with an energy of 86 MeV at the height of the shower maximum.

2.2.3.6 Event Separation and Characterization

Even for a strong γ -ray source as the Crab Nebula, the number of hadron events that survive image cleaning is ~ 3 orders of magnitude larger than the one of gamma rays. The purpose of the single-telescope and stereo image parametrization is to separate γ -like showers from the rest.

For stereo observations we use RFs for γ /hadron separation and direction reconstruction, and LUTs for the energy estimation. To create the RFs and LUTs, we use a program called `coach`. For single-telescope, we use RFs for γ /hadron separation, direction reconstruction and energy estimation and all of them are produced by a program called `osteria`.

γ /hadron separation To evaluate how similar to a γ -ray shower an event is, we use a multi-variate algorithm based on decision trees called *Random Forest (RF)* (Albert et al. 2008). It uses training samples representing γ -ray showers and hadronic showers. As it is shown in Fig. 2.21, at this stage the MC sample is split in two subsamples: the *train* subsample, used to teach the RF how γ -like events look like, and the *test* subsample, that is used later in the analysis to calculate the collection area and migration matrix and has to be different from the *train* sample not to have a biased result. A sample of real hadron data is also needed here to train the RF on what are the parameters of hadron-like events. The hadron sample must match the Z_d conditions at which the RF needs to be trained. As the hadron to γ -ray rate is large, any sample of a non-detected source or a weak one is suitable to train the RF.

The algorithm works as follows: we select P parameters to discriminate between gamma rays and hadrons, then the training RF grows a number n (by default $n = 100$) of decisional trees. The growing works as follows: One of the P parameters is randomly selected, and the data sample (containing gamma and hadron events) is separated in two subsamples (branches) based on this parameter. The cut of the parameter that better separates the sample is found by the RF by minimizing the Gini index (Gini 1921):

$$Q_{\text{Gini}} = 4 \frac{N_\gamma}{N} \frac{N_h}{N} \quad (2.8)$$

where N_γ is the number of gammas, N_h the number of hadrons and N the total number of events. The procedure is repeated by randomly selecting another parameter and further separating the subsample until the final branch only contains events of one of the populations. This branch is assigned a 1 (or 0) depending if the events are hadrons (or gammas).

We apply the RF to the data sample using the program `melibe`. Every event has to pass through all the n decisional trees previously grown. The event is then assigned a *hadronness* value 0 or 1 depending if it ends up in a γ -branch or a hadron-branch. The final *hadronness* value of the event is given by the mean value of the *hadronness* of all the trees:

$$h = \sum_{i=1}^n \frac{h_i}{n} \quad (2.9)$$

where h_i is the *hadronness* resulting from passing the event through the i -th branch and h is the final *hadronness* assigned to the event.

Arrival direction reconstruction The determination of the arrival direction of the incoming γ -ray is easy for stereo observations (using the *crossing method* introduced in Sect. 2.2.3.5). For single-telescope observations we need to resort to the so-called “Disp” method (Fomin et al. 1994; Lessard et al. 2001). The Disp method has also proven to improve the arrival direction reconstruction for stereo observations, therefore it is used in stereo analysis as well.

The source position in a γ -ray shower produces an elliptical image at the camera. The distance from the image CoG to the source position is known as *disp* and can be determined using the following formula:

$$disp = A(size) + B(size) \frac{width}{length + \eta(size)leakage2} \quad (2.10)$$

where $A(size)$, $B(size)$ and $\eta(size)$ are second order polynomials of $\log(size)$ whose coefficients are determined using MC gamma rays. As illustrated in the left panel of Fig. 2.27, the source may be at two different positions for the same *disp*. The directional parameters introduced in Sect. 2.2.3.3 can be used to break this degeneracy.

This parametrization is not very efficient at high energies because many images are truncated. The method used for single-telescope direction reconstruction is a method based on the RF algorithm trained with MC gamma rays whose *disp* parameters are known. The RF is grown on a similar way as that explained for the γ /hadron separation, but the minimized parameter is the *disp* variance of each of the branches.

For stereo analysis, the *crossing method* gives a good estimate of the γ -ray arrival direction, but this method fails for parallel showers and very small reconstructed images. An improved method uses the *disp* information of both reconstructed

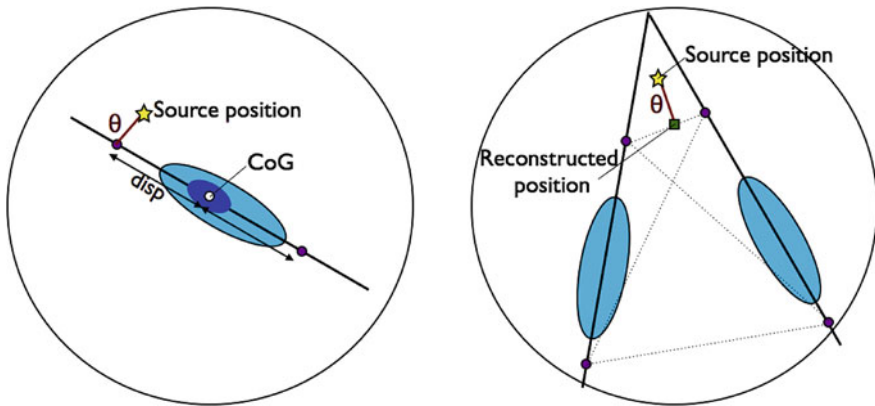


Fig. 2.27 Disp reconstruction method for single-telescope (left panel) and stereo (right panel)

showers. Figure 2.27 (right panel) illustrates this method. First, we calculate the four estimates of the source position ($disp$) for the shower images (two per image). Secondly, we calculate the distance between each pair of source position estimates from different images (the dotted lines in the right panel of Fig. 2.27). Thirdly, we select the pair at the smallest distance which is the one taken for calculating the reconstructed direction of the shower. If this distance is larger than 0.22° , the reconstruction is not valid. Finally, the reconstructed direction is the average between the chosen pair of positions weighted with the number of pixels in each image. The θ distance shown in Fig. 2.27 (right panel) is the angular distance between the reconstructed and the true position of the source. Its distribution can be used to extract the γ -ray signal as it will be shown in Sect. 2.2.3.7.

The $disp$ method helps in the reconstruction of events with large impact parameter. Considering the 2-dimensional distribution of reconstructed arrival directions, we define the **angular resolution** as the angle that encloses 68 % of the events. The left panel of Fig. 2.28 shows the angular resolution of MAGIC as a function of the energy obtained using MC γ -ray events. It reaches a value of 0.11° at 250 GeV and it is as good as 0.06° above a few TeV.

Energy estimation For single-telescope observations, the energy estimation is performed by means of a RF. The RF is grown in a similar way as previously mentioned, but in this case we select different parameters and aim at minimizing not the Gini index, but the variance of E_{true} of the events in each of the subsamples.

In the stereo analysis instead we use LUTs. LUTs are filled with the true energy (E_{true}) and the RMS of MC simulated gamma rays. They are binned in *size* and *impact parameter*/ r_C , where r_C is the Cherenkov radius defined in Sect. 2.2.3.5. The estimated energy (E_{est}) of each event is the weighted average of both telescopes where the weight is given by the RMS of the bin. Finally, we apply an empirical correction proportional to the $\cos(Zd)$.

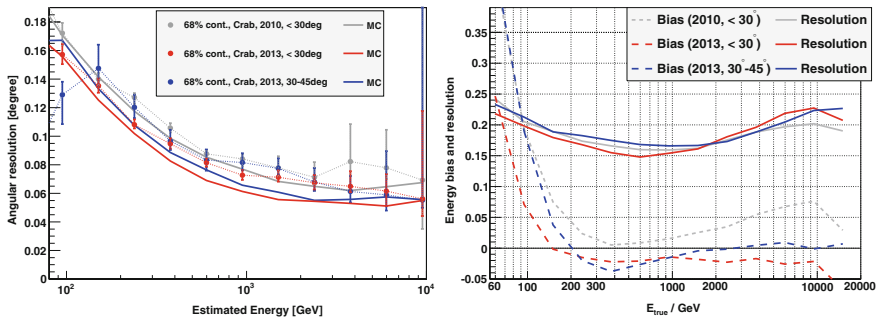


Fig. 2.28 MAGIC angular resolution (*left panel*), energy resolution and energy bias (*right panel*). 2010 refers to the period before the readout upgrade to DRS4 and 2013 to the period after. Plots taken from Aleksić et al. (2014g)

The **energy bias** is defined as:

$$E_{\text{bias}} = \frac{E_{\text{est}} - E_{\text{true}}}{E_{\text{true}}} \quad (2.11)$$

to compute the energy bias for a given energy bin, we fit a gaussian to the energy biases of the individual events. The energy bias of the system is the mean of that gaussian. The **energy resolution** is defined as the σ of the gaussian. A plot comparing the current MAGIC energy resolution and bias at low and medium Zd and the resolution and bias previous to the upgrade are shown in the right panel of Fig. 2.28. We can see that the energy resolution is as good as 15 % at few hundred GeV. It worsens for higher energies because the impact parameter grows and truncated images become more frequent. For low energies it also gets worse due to misreconstructed images. The energy bias is close to 0 for energies >100 GeV, however it rapidly increases below these energies due to threshold effects.

Finally, the **energy threshold** of the telescope is defined as the peak of the simulated energy distribution for a source with photon spectral index 2.6. It can be evaluated at several stages of the analysis, but most relevant is the threshold obtained after applying analysis cuts because it corresponds to the energy at which most of the events used for analysis are recorded. Events with energies below the threshold can be reconstructed as well, but the spectral points have significant errors. After applying a cut of 50 phe, *hadronness* and θ^2 cuts, the current energy threshold of the MAGIC telescope is ~ 75 GeV for low Zd observations. A plot showing the energy distribution of gamma rays after analysis cuts of MAGIC for two Zd ranges is shown in Fig. 2.29.

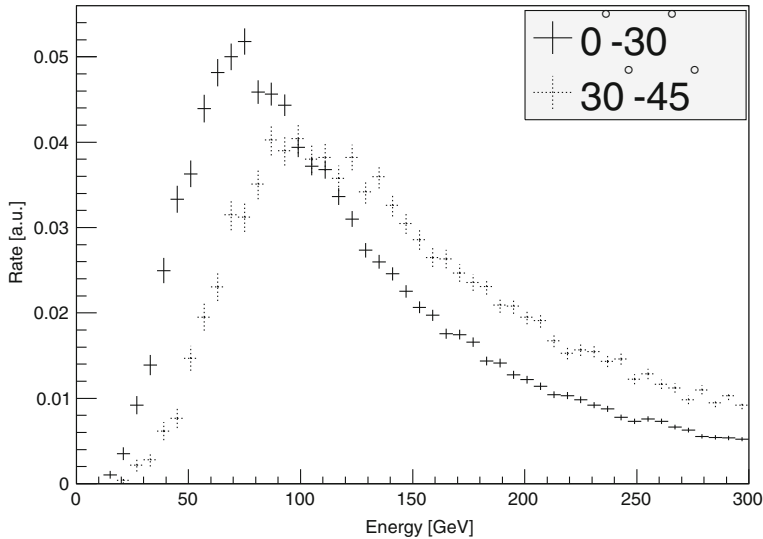


Fig. 2.29 Rate of γ -ray events surviving analysis cuts for a Zd range between $0-30^\circ$ (solid lines) and between $30-45^\circ$ (dashed lines). Plot taken from Aleksić et al. (2014g)

2.2.3.7 Signal Extraction and Sensitivity

Once we have evaluated *hadronness*, reconstructed energy and direction of the events, we can evaluate if the data sample contains a signal. For stereo analysis, a program called `odie` computes the angular distance θ between the reconstructed and the expected source position for every event and fills the so-called *signal histogram*, binned in θ^2 . Assuming that the acceptance of the camera is the same for regions close to the center, the background would be flat over the whole histogram, while the γ -like events would accumulate at small values of θ^2 . Only events that survive some other previously defined cuts in *hadronness*, *size*... are included in the signal histogram. These cuts can be optimized on an independent data sample (usually Crab Nebula data). The current standard set of cuts used for the detection in several energy ranges can be found in Table 2.2.

Once we have filled the signal histogram with the events surviving all the cuts and the signal region has been defined, we count the number of events in the signal region, N_{on} . These events are not only gamma rays coming from the source, but also γ -like hadrons, e^\pm and diffuse gammas. In order to estimate how many hadron events are inside the signal region, we fill a different θ^2 histogram, the *background histogram*, where θ is now the distance from the reconstructed position to the “off position”, which is the position that is situated at the same distance as the source from the center of the camera, but on a different region (see Fig. 2.20). The γ -ray events having small θ^2 with respect to the source position, are also included in the background histogram as it can be seen in Fig. 2.30. As it was shown in Fig. 2.20b, we can take more than one equivalent region to calculate the number of number of hadrons that there is in the signal region. Finally, the number of excess N_{ex} is given by:

$$N_{\text{ex}} = N_{\text{on}} - \alpha N_{\text{off}} \quad (2.12)$$

where α is $1/(\text{number of OFF regions})$. An example of a θ^2 histogram is shown in Fig. 2.31.

The significance of the signal is usually calculated using Eq. 2.17 from Li and Ma (1983):

$$\sigma_{\text{LiMa}} = \sqrt{2 \left(N_{\text{on}} \ln \left[\frac{1 + \alpha}{\alpha} \left(\frac{N_{\text{on}}}{N_{\text{on}} - N_{\text{off}}} \right) \right] + N_{\text{off}} \ln \left[(1 + \alpha) \left(\frac{N_{\text{off}}}{N_{\text{on}} - N_{\text{off}}} \right) \right] \right)} \quad (2.13)$$

Table 2.2 Standard cuts for the different energy ranges in the MAGIC analysis

Energy range	Hadronness	θ^2	Size [M1]	Size [M2]	E_{est}
Low energies	<0.28	<0.02	>60	>60	—
Medium-to-high energies	<0.16	<0.009	>300	>300	—
High energies	<0.1	<0.007	>400	>400	>1000

Fig. 2.30 Sketch illustrating how θ is calculated respect to the source and off positions

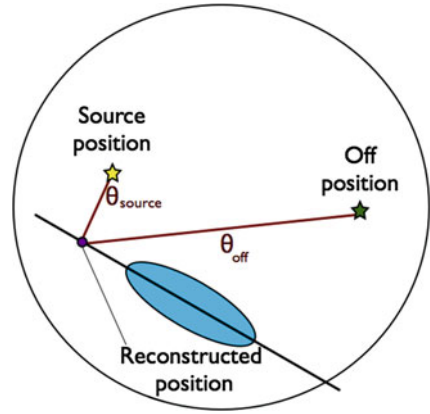
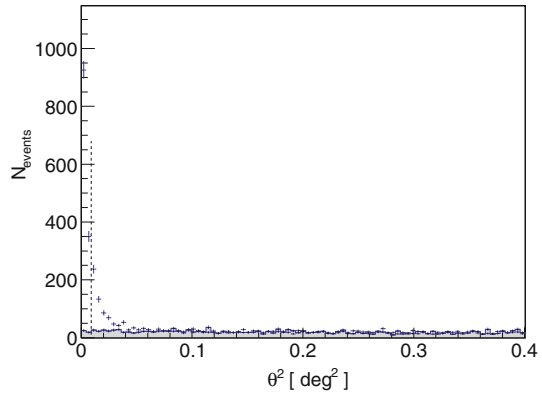


Fig. 2.31 θ^2 distribution obtained for the Crab Nebula after medium-to-high hadronness and size cuts (Table 2.2). The grey histogram is filled with a θ^2 calculated with respect to the off position. The points correspond to an histogram filled with a θ^2 calculated with respect to the source position



but it can also be given as:

$$\sigma_{N_{ex}/\sqrt{N_{off}}} = \frac{N_{ex}}{\sqrt{N_{off}}} \quad (2.14)$$

which is a Gaussian approximation of (2.13).

Sensitivity The sensitivity of the instrument is calculated as the minimum signal that can be detected in 50h with 5σ using the significance $\sigma_{N_{ex}/\sqrt{N_{off}}}$. It is usually expressed in units of the Crab Nebula flux.

Given an observation of the Crab Nebula where a number of observed excesses N_{ex} , background events in the signal region N_{off} in a time t are observed, the significance in a time $t_0 = 50$ h is given by:

$$\sigma_{N_{ex}/\sqrt{N_{off}}}(t_0) = \sqrt{\frac{t_0}{t}} \frac{N_{ex}}{\sqrt{N_{off}}} \quad (2.15)$$

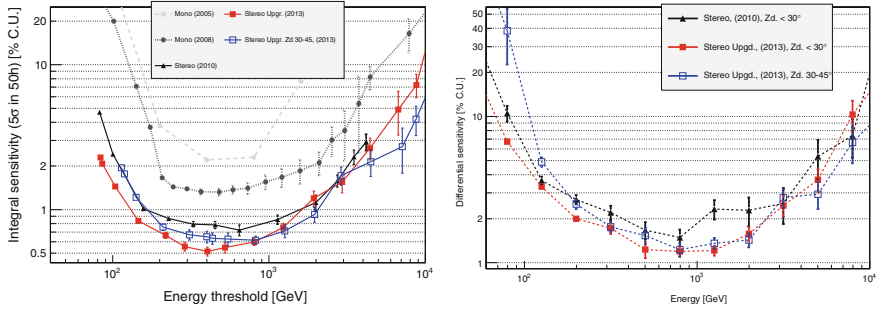


Fig. 2.32 MAGIC integral (left panel) and differential (right panel) sensitivity as a function of energy. Red curves correspond to the current MAGIC sensitivity for low Z_d observations (between 0°–30°) and the blue one represents the current MAGIC sensitivity for the Z_d range between 30°–45°. For comparison, the black curve represents MAGIC sensitivity before the installation of the DRS4 readout and the grey dotted and the grey dashed curves the sensitivity of MAGIC in single-telescope mode, for MUX and Siegen readouts respectively. Plots taken from Aleksić et al. (2014g)

And the sensitivity, given as the minimum flux that can be detected in 50h with a significance 5σ in Crab units is:

$$Sensitivity = \frac{5\sigma}{\sigma_{Nex/\sqrt{Noff}}(t_0)} \quad (2.16)$$

The sensitivity is useful to compare the performance of different instruments and to estimate the flux that can be detected for a given amount of observation time.

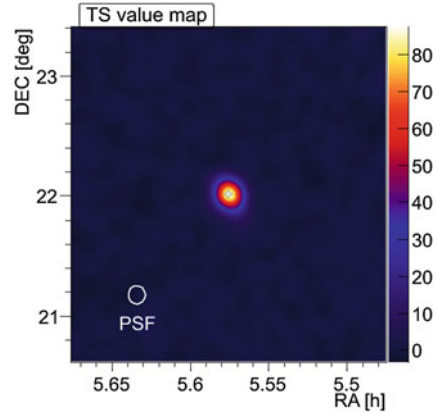
There are two ways to give the sensitivity of an experiment: we can search for a set of cuts (*hadronness*, *size*, θ^2 ...) that give the best sensitivity above a given energy threshold. This is the so-called **integral sensitivity**. We can also search for the set of cuts that give the best sensitivity in a given energy range and compute the **differential sensitivity** in that range. The current MAGIC integral and differential sensitivities are shown in Fig. 2.32.

2.2.3.8 Skymaps

Skymaps are two-dimensional histograms containing the arrival direction of all the γ -ray candidates. To select the events going to the histogram, the standard cuts applied to the data are the same as those shown in Table 2.2. They are produced using the source-independent information provided by the *disp* method. The program producing the skymaps in MAGIC is called *caspar*.

The most difficult task to produce a reliable skymap is the background estimation. Due to the inhomogeneities in the pixel response, stars in the FoV and observations at different Z_d and Az, the background estimation is affected. An advantage of *wobble* observations is that background can be extracted from the same data sample

Fig. 2.33 TS skymap of the Crab Nebula



as the signal. To avoid contamination from the signal region and correct the camera inhomogeneities, for each wobble position the camera is divided in two halves and the γ -ray candidates from the half that does not contain the source are accepted for the background skymap. For calculating the significance of a signal in a skymap, we use the Test Statistics (TS) significance, which is the LiMa significance applied on a smoothed and modeled background estimate.

An example of a TS skymap can be seen in Fig. 2.33. When we have the signal and background skymaps, we subtract them to obtain the excesses histogram. This histogram is smoothed using the instrument's PSF added in quadrature with a Gaussian kernel to smear the number of excesses obtained. Finally, the σ_{smooth} used to smear the excesses histogram is given by:

$$\sigma_{\text{smooth}} = \sqrt{\sigma_{\text{PSF}}^2 + \sigma_{\text{Kernel}}^2} \quad (2.17)$$

The Gaussian kernel is usually taken equal to the PSF, so finally $\sigma_{\text{smooth}} = \sqrt{2}\sigma_{\text{PSF}}$.

2.2.3.9 Spectrum and Light Curve

Spectrum The γ -ray differential spectrum of a given source is the number of photons per unit of energy, time and area. It can be written as:

$$\frac{d\phi}{dE} = \frac{dN_{\gamma}(E)}{dE dA(E) dt} \quad (2.18)$$

To calculate it we need to compute the number of gammas in a given energy range, the collection area of the instrument and the effective observation time we spend on a given source. In MAGIC we use two dedicated programs to calculate the spectrum: the first one is called `fluxlc` (FLUX and Light Curve) and is used for

single-telescope data, the second one is called `flute` (FLUX vs. Time and Energy) and is a simplified and advanced version of the first one that works for stereo data only. These programs use the `melibe` output of the data to calculate the *number of gammas* in each energy bin and the *effective time*. It also uses the `melibe` output of the MC gamma rays to calculate the *collection area* and the best cuts to extract the number of excesses in each energy bin (the scheme of this process is shown in Fig. 2.21).

Number of gammas: $N_\gamma(E)$ is the number of excess events $N_{\text{ex}} = N_{\text{on}} - N_{\text{off}}$ in the energy range E . It is calculated in a similar way as it is done for the signal detection described in Sect. 2.2.3.7. A set of cuts (*hadronness*, θ^2) is selected in each energy bin, and the number of excess computed. The set of cuts is determined using MC in the following way: an efficiency is defined, and we change *hadronness* and θ^2 cuts until the number of surviving events exceeds this efficiency for each energy bin. These cuts are usually looser than the ones used to detect a signal, because that generally results in a better agreement of real and MC data and assures a better estimate of the *collection area*.

Effective time: It is the effective time of observation of a source. If we assume that the arrival time distribution of cosmic events follows a Poissonian distribution, the time difference between the arrival time of an event and the next one Δt , behaves exponentially. Given the Poissonian probability of observing n events in a time t for the event rate λ :

$$P(n, t) = \frac{(\lambda t)^n e^{-\lambda t}}{n!} \quad (2.19)$$

The probability that an event comes after a time t' is equal to the probability of observing 0 events in a time $t < t'$:

$$P(t' > t) = P(0, t) = e^{-\lambda t} \quad (2.20)$$

Since this probability can also be written as:

$$P(t' > t) = \int_t^\infty \frac{dP(t' = t)}{dt} dt \quad (2.21)$$

Therefore, the time evolution of the probability is given by:

$$\frac{dP(t' = t)}{dt} = \lambda e^{-\lambda t} \quad (2.22)$$

The event rate is given by the product of the time evolution probability times the number of recorded events N_0 :

$$\frac{dN}{dt} = N_0 \lambda e^{-\lambda t} \quad (2.23)$$

being λ the rate of events recorded by the telescope that can be obtained from fitting to an exponential function the distribution of difference on arrival times between events Δt . An example of the distribution of Δt for a typical observation can be seen in Fig. 2.34. Finally, the effective time can be written as the total number of events divided by the event rate:

$$t_{\text{eff}} = \frac{N_0}{\lambda} \quad (2.24)$$

The reason that the effective time is not coincident with the time elapsed between the beginning and the end of the observation is that there might be gaps in data taking (between runs) and that the data taking has a certain dead time after each event (as it was explained in Sect. 2.2.1.7).

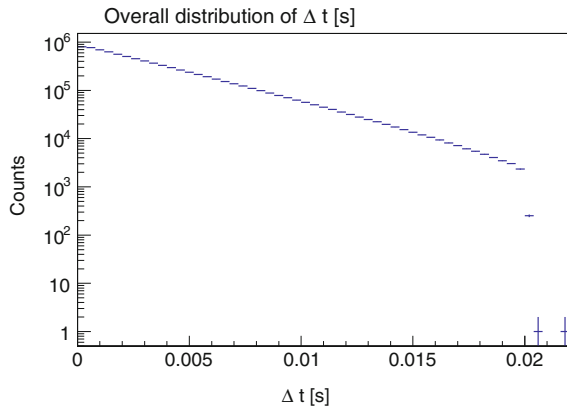
Collection area: It is the geometrical area around the instrument where the gamma rays are detected. It is calculated using MC gamma rays and results from dividing the number of detected gamma rays surviving analysis cuts by the number of simulated gamma rays in a given energy range multiplied by the simulated area, or the area of an ideal telescope that would detect all the simulated gamma rays. Its mathematical expression is:

$$A_{\text{eff}}(E) = A_{\text{sim}} \frac{N_{\text{sel}}(E)}{N_{\text{sim}}(E)} \quad (2.25)$$

where A_{sim} is the simulated area, $N_{\text{sim}}(E)$ the number of simulated events in a given energy range and $N_{\text{sel}}(E)$ the number of events surviving cuts in the mentioned energy range. Equation 2.25 is only true if the MC gamma rays are simulated with the spectrum of the γ -ray source. Otherwise each event has to be weighted as it is explained in Appendix A.1.

The effective area depends on the Z_d of the observations, being larger for larger Z_d because the shower is produced further away in the atmosphere, as it was explained in Sect. 2.1.3. An example of the effective area covered by MAGIC at the trigger and analysis level is shown in Fig. 2.35. The simulated area in MAGIC is currently a

Fig. 2.34 Distribution of time differences between events



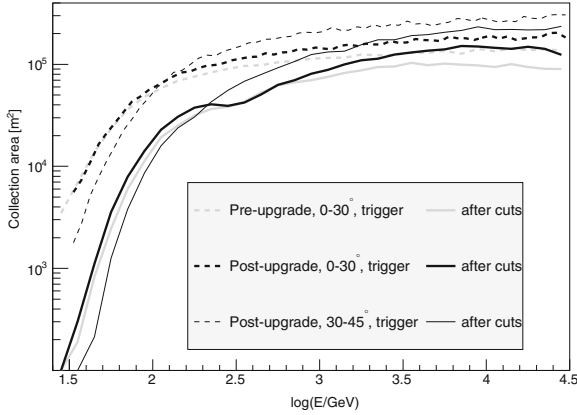


Fig. 2.35 Collection area before (*dashed lines*) and after (*solid lines*) applying analysis cuts. The collection area for the telescope equipped with the DRS4 readout and Zd range between 0–30° is represented with a thick black line and for the range between 30–45° with a thin *black line*. For comparison, the collection area for the period before the MAGIC upgrade is also included in *grey*. Plots taken from Aleksić et al. (2014g)

circle whose maximum radius, for each of the Zd ranges where the MC gamma rays are simulated can be found in Table 2.3.

Light curve: Light curves show integral fluxes in a given energy range and in bins of time. The differential energy spectrum (Eq. 2.18) is calculated for each of the time intervals, and then integrated over the energy range:

$$\phi = \int_{E_0}^{E_1} \frac{d\phi}{dE} [\text{cm}^{-2}\text{s}^{-1}] \quad (2.26)$$

Upper limits: Upper Limits (ULs) on the flux are computed when no significant γ -ray signal is found. Using the number of measured excess events N_{ex} , the number of off events N_{off} and selecting a Confidence Level (C.L.) and systematic error, we can calculate an U.L. to the number of expected signal events N_{ul} using the method described in Rolke et al. (2005). The C.L. usually used to calculate MAGIC ULs is 95 % and the systematic error assumed is 30 %. N_{ul} is the UL on the maximum number of expected events according to the measurements performed and the confidence level

Table 2.3 Maximum impact parameters simulated for each Zd range

Zd range [°]	Maximum impact [m]
05–35	350
35–50	500
50–62	700
62–70	1000

defined. As we do not have any information about the source, we also have to assume a spectral shape, usually a power-law with spectral index $\Gamma = 2.6$.

$$\phi(E) = K S(E) = \left(\frac{E}{E_0} \right)^{-\Gamma} \quad (2.27)$$

The integral flux above an energy E_{\min} can be written as:

$$\int_{E_{\min}}^{\infty} \phi(E) dE = K \int_{E_c}^{\infty} S(E) dE = \frac{N_{\text{ul}}}{\int_{E_{\min}}^{\infty} \int_0^{t_{\text{obs}}} A(E) dE dt} \quad (2.28)$$

where t_{obs} is the observation time. Finally, the UL on the integral flux K_{ul} can be written as:

$$K_{\text{ul}} < \frac{N_{\text{ul}}}{T \int_{E_{\min}}^{\infty} S(E) A(E) dE} \quad [\text{TeV}^{-1} \text{cm}^{-2} \text{s}^{-1}]. \quad (2.29)$$

2.2.3.10 Unfolding

Due to the non-idealities of the detectors, experimental results get usually distorted. To correct for the finite resolution of our telescope, we apply an unfolding procedure. In IACTs, events have an estimated energy, but their true energy is not known. Defining the detector response function to a measured quantity y (E_{est}) from a true quantity x (E_{true}) as $M(x, y)$, the measured distribution $g(y)$ can be written as a function of the true distribution $f(x)$:

$$g(y) = \int M(x, y) f(x) dx + b(y) \quad (2.30)$$

where $b(y)$ accounts for a possible background contribution in the measurement. Since the data is binned in bins of E_{true} and E_{est} , the equation can also be written:

$$g_i = \int M_{ij} f_j + b_i \quad (2.31)$$

In the case of MAGIC, the tensor M_{ij} is given by the *migration matrix* of the detector and can be calculated from simulated γ -ray MC. It basically represents the probability that an event with E_{true} belonging to bin j ends up in bin i of the E_{est} distribution. The easier way to solve this problem would be to invert M_{ij} , but this is sometimes not possible. In this case, the best way to solve this problem is the least square minimization method, finding the value that minimizes the χ_0^2 . This, however, gives unstable results, so a regularization term is added:

$$\chi^2 = \chi_0^2 + \frac{\omega}{2} \chi_0^2 + \text{Reg}(f) \quad (2.32)$$

where $Reg(f)$ is the regularization and ω is the inverse of the regularization strength, which is a way to adjust the weight given to the regularization within the χ^2 equation. Large values of ω imply less regularization and usually produce spectra with fluctuations, but small values of ω produce too smooth unfolded distributions that can deviate from the data. The determination of an appropriate value for the regularization is very important when producing an unfolded spectrum. There are several methods to compute the regularization in MAGIC, they are described in Schmelling (1994), Bertero (1989), Tikhonov & Arsenin (1977)

There is another way of unfolding the data, the so-called *forward unfolding* method. It assumes a-priori the spectral shape that will be followed by the measurement, and minimizes the χ_0^2 with respect to these parameters. This is generally done analytically, forcing the solution to be continuous. The result is the best fit to the a-priori defined parameters, therefore no spectral points are available. Since no regularization is used, the result from the forward unfolding only depends on the assumed spectral shape.

The convergence on the result of all the unfolding methods has to be carefully checked. The spectra results shown by MAGIC are usually given using the *forward unfolding* method, although to produce the spectral points one of the other methods is used.

2.3 CTA

The Cherenkov Telescope Array (CTA) is an initiative to build a next generation ground-based VHE γ -ray instrument. It is proposed as an open observatory and it currently (May 2015) gathers about 1300 scientists from 29 countries worldwide. It is planned to have two sites, one in the southern hemisphere focused on galactic physics and another one in the northern hemisphere, mainly focused on extragalactic physics and transient events. The final site selection for both sites is expected to take place during the year 2015. An artist view of the CTA array is shown in Fig. 2.36. The technical objectives of the future-generation CTA can be summarized as:

- Achieve the lowest possible energy threshold by an IACT to be sensitive to transient phenomena such as blazars, GRBs, novae and any other phenomena that emits photons in the $\mathcal{O}(10\text{--}100)$ GeV band and lasts for days to weeks. This purpose will be achieved by the use of LSTs with their large reflectors able to collect the few photons produced by $\mathcal{O}(10)$ GeV cascades. LSTs are designed to work in stereo, which translates in an increase in the collection area of the array and a more powerful gamma/hadron separation. The latter is especially important at the lowest energies where γ -like showers are similar to cascades generated by hadrons or accidental triggers.

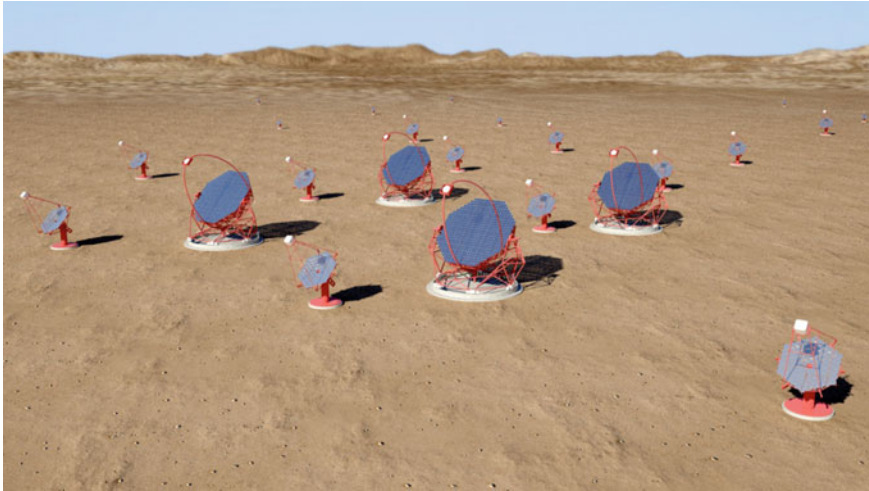
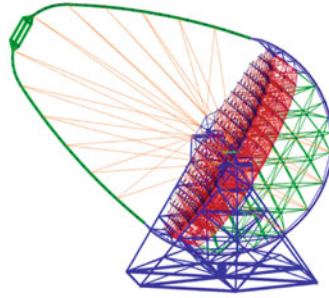


Fig. 2.36 CTA design concept. One can see four LSTs in the center of the array and they are surrounded by MSTs. SSTs are placed farther away from the center of the array to extend the overall collection area. Image courtesy G. Perez, SMM, IAC

- Improve the sensitivity at the medium energy band $\mathcal{O}(0.1\text{--}1)\text{TeV}$ down to a few mCrab. This is achieved by collecting more photons and improving the angular and energy resolution for a better background rejection. The improved cameras and the increased number of MSTs with respect to the current arrays using similar telescopes (HESS, VERITAS) will make it possible.
- As the flux of γ -ray photons at $\mathcal{O}(10)\text{TeV}$ is very small, to significantly detect them at these energies one has to increase the collection area. Background suppression at these energies is not a problem because of the steepness (power-law with a 2.7 photon spectral index) of the hadron spectrum. Several SSTs will be located in the outer parts of the array. They have high energy threshold ($\mathcal{O}(1)\text{TeV}$), but their only purpose is to extend the collection area of the array to collect the maximum number of VHE photons at energies $>10\text{TeV}$.

There are mainly three telescope types:

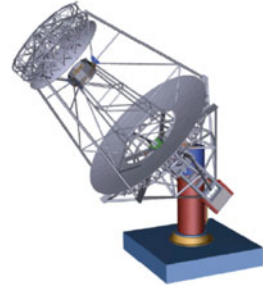
- **Large Size Telescope (LST):** They are designed to be light-weighted to achieve fast repositioning to catch GRBs. The structure is made of carbon-fiber tubes holding a tessellated parabolic reflector of 23 m diameter. The current design has a 27.8 m focal length, 4.5° FoV and 0.1° PMTs as pixels (Acharya et al. 2013). A maximum of four telescopes will be placed in the center of the array of each observatory. A drawing of the LST design can be seen in Fig. 2.37a.
- **Medium Size Telescope (MST):** They are designed to have 12 m Davies-Cotton reflectors. The current design is to have 17 m focal length, $7\text{--}8^\circ$ FoV and 0.18° PMT pixels. In the order of thirty MSTs will surround the LSTs in each site. A picture of the MST prototype constructed in DESY Berlin is shown in Fig. 2.37b



(a) LST drawing.



(b) Single-mirror MST prototype in DESY Berlin.



(c) Dual-mirror MST SCT prototype design.



(d) Single-mirror SST prototype in Krakow.



(e) Dual-mirror SST prototype on Mount Etna.

Fig. 2.37 Prototypes and designs of the different telescope types for CTA

There is also a plan to construct a double mirror SCT to extend the southern array with a maximum of 36 telescopes of this type (Vassiliev & Fegan 2008). They are currently planned to have a 10° FoV allowing a small plate scale that can be filled with smaller pixels such as SiPM. A drawing of the SCT telescope design is shown in Fig. 2.37c.

- **Small Size Telescope (SST):** A variable number between 35–70 SSTs will be placed in principle only in the southern observatory, focused on galactic physics and interested in the highest γ -ray energies. Several solutions have been designed to reduce the cost and be able to construct such a large number of telescopes. A prototype using the traditional Davies-Cotton optics with a 1 m reflector was built in Kraków and is shown in Fig. 2.37e. The usage of the Schwarzschild-Couder optics has also been developed for this type of telescopes and a picture of the 2 m primary reflector ASTRI SST prototype constructed by INAF is shown in Fig. 2.37d.

The physic cases are several (Acharya et al. 2013) and can be summarized as:

1. Study the origin and propagation of cosmic rays
2. Understand particle acceleration in several objects such as pulsars, PWNe, SNRs, novae, black holes and any other object where extreme acceleration takes place.
3. Search for new physics beyond the Standard Model and study the nature of dark matter.

The duration of this thesis took place during the Design and Prototyping phases of the CTA schedule, therefore all the contribution to the CTA project is technical. CTA is expected to start scientific operation in 2018, although the full array is not expected to be completed before 2020.

References

- Abramowski A et al (2014a). [arXiv:1411.7568](#)
 Acharya BS et al (2013) *Astropart Phys* 43:3
 Aharonian F et al (1997b) *Astropart Phys* 6:343
 Albert J et al (2008) *Nucl Instrum Methods Phys Res A* 588:424
 Aleksić J et al (2014f). [arXiv:1409.6073](#)
 Aleksić J et al (2014g). [arXiv:1409.5594](#)
 Aleksić J et al (2014a) *Science* 346:1080
 Aliu E et al (2008) *Science* 322:1221
 Aliu E et al (2009) *Astropart Phys* 30:293
 Barrio JA, et al (1998) *MPI-PhE* 98–05
 Bartko H et al (2005) *Nucl Instrum Methods Phys Res A* 548:464
 Bertero M (1989) *Linear inverse and ill-posed problems*, vol 75. Academic Press, New York, pp 1–120
 Biland A et al (2008) *Int Cosmic Ray Conf* 3:1353
 Bitossi M (2009) *Ultra-fast sampling and readout for the MAGIC-II telescope data acquisition system*, Ph.D. thesis
 Blackett PMS (1948) *The emission spectra of the night sky and aurorae*, 34
 Bretz T et al (2014). [arXiv:1403.3573](#)
 Bretz T et al (2009) *Astropart Phys* 31:92
 Cherenkov P, *Doklady CR* (1934) *Akad. Sci. URSS* 2:451
 Elterman L (1964) *Appl Opt* 3:745
 Engel R et al (2011) *Annu Rev Nucl Part Sci* 61:467
 Fomin VP et al (1994) *Astropart Phys* 2:137

- Fruck C et al (2014). [arXiv:1403.3591](#)
- García JR, et al (2014). [arXiv:1404.4219](#)
- Gini C (1921) Econ J 31:22
- Heck D et al (1998) CORSIKA: a Monte Carlo code to simulate extensive air showers. (Forschungszentrum Karlsruhe GmbH)
- Hillas AM (1985) Int Cosm Ray Conf 3:445
- Hofmann W et al (1999) Astropart Phys 12:135
- Jelley JV et al (1963) QJRAS 4:275
- Lessard RW et al (2001) Astropart Phys 15:1
- Li T-P et al (1983) ApJ 272:317
- Lombardi S (2011) Int Cosm Ray Conf 3:266
- Longair MS (1992) High energy astrophysics. Cambridge University Press, Cambridge
- López M (2013) Proc ICRC, vol 692
- Lucarelli F et al (2008) Nucl Instrum Methods Phys Res A 589:415
- Majumdar P et al (2005) Int Cosm Ray Conf 5:203
- Mirzoyan R et al (1994) MPI-PhE/94-35
- Mirzoyan R (1997) Int Cosm Ray Conf 7:265
- Mirzoyan R et al (2002) IEEE Trans Nucl Sci 49:2473
- Moralejo A (2000) Búsqueda de fuentes cósmicas de radiación gamma de muy alta energía con el detector AIROBICC, Ph.D. thesis
- Nakajima D et al (2013) Proc ICRC, vol 787
- Oser S et al (2001) ApJ 547:949
- Paoletti R et al (2007) IEEE Trans Nucl Sci 54:404
- Rissi M et al (2009) IEEE Trans Nucl Sci 56:3840
- Rolke WA et al (2005) Nucl Instrum Methods Phys Res A 551:493
- Schmelling M (1994) Nucl Instrum Methods Phys Res A 340:400
- Schmidt F (2015) CORSIKA shower images. <http://www.ast.leeds.ac.uk/fs/showerimages.html>
- Sitarek J et al (2013) Nucl Instrum Methods Phys Res A 723:109
- Staszak D (2014) Nucl Instrum Methods Phys Res A 742:212
- Tescaro D et al (2009). [arXiv:0907.0466](#)
- Tescaro D et al (2013). [arXiv:1310.1565](#)
- Tikhonov A et al (1977) Solutions of ill-posed problems., Scripta series in mathematics Winston, Great Falls
- Vassiliev VV et al (2008) Int Cosm Ray Conf 3:1445
- Wagner R (2006) Measurement of VHE γ -ray emission from four blazars using the MAGIC telescope and a comparative blazar study, Ph.D. thesis
- Yao W-M et al (2006) J Phys G Nucl Phys 33:1
- Zanin R (2011) Observation of the Crab pulsar wind nebula and micro quasar candidates with MAGIC, Ph.D. thesis
- Zanin R et al (2013) Proc ICRC, vol 773

Very-high-energy Gamma-ray Observations of Pulsar
Wind Nebulae and Cataclysmic Variable Stars with
MAGIC and Development of Trigger Systems for IACTs

López Coto, R.

2017, XXXVIII, 217 p. 127 illus., 101 illus. in color.,

Hardcover

ISBN: 978-3-319-44750-6